



OPEN ACCESS

EDITED BY

Qiuming Pei,
Southwest Jiaotong University, China

REVIEWED BY

Hua-Wen Cao,
China Geological Survey, China
Kit Lai,
Fortescue Metals Group, Australia
Huan Li,
Central South University, China

*CORRESPONDENCE

Chenghui Wang,
✉ wangchenghui@mail.cgs.gov.cn
Yubin Li,
✉ liyb73@163.com

SPECIALTY SECTION

This article was submitted to Structural
Geology and Tectonics,
a section of the journal
Frontiers in Earth Science

RECEIVED 31 August 2022

ACCEPTED 20 December 2022

PUBLISHED 06 January 2023

CITATION

Li Y, Wang C, Li Y, Sun Y, Puchi M, Zhang X,
Lamu G and Yang Z (2023), Genesis of the
Abunabu antimony deposits in the Tethys
Himalayan metallogenic belt: Evidence
from He–Ar and S isotopes of stibnite.
Front. Earth Sci. 10:1033124.
doi: 10.3389/feart.2022.1033124

COPYRIGHT

© 2023 Li, Wang, Li, Sun, Puchi, Zhang,
Lamu and Yang. This is an open-access
article distributed under the terms of the
[Creative Commons Attribution License
\(CC BY\)](https://creativecommons.org/licenses/by/4.0/). The use, distribution or
reproduction in other forums is permitted,
provided the original author(s) and the
copyright owner(s) are credited and that
the original publication in this journal is
cited, in accordance with accepted
academic practice. No use, distribution or
reproduction is permitted which does not
comply with these terms.

Genesis of the Abunabu antimony deposits in the Tethys Himalayan metallogenic belt: Evidence from He–Ar and S isotopes of stibnite

Yang Li^{1,2}, Chenghui Wang^{2*}, Yubin Li^{3*}, Yan Sun², Mima Puchi⁴,
Xudong Zhang⁵, Gesang Lamu⁶ and Zong Yang⁷

¹College of Earth Sciences, Chengdu University of Technology, Chengdu, Sichuan, China, ²Institute of Mineral Resources, Chinese Academy of Geological Sciences, Beijing, China, ³College of Engineering, Tibet University, Lhasa, Tibet, China, ⁴Regional Geological Survey Team, Tibet Bureau of Geological Exploration and Development, Lhasa, Tibet, China, ⁵No.5 Geological Brigade, Tibet Bureau of Geological Exploration and Development, Golmud, Qinghai, China, ⁶No.6 Geological Brigade, Tibet Bureau of Geological Exploration and Development, Lhasa, Tibet, China, ⁷Geological Survey Institute of Tibet Autonomous Region, Lhasa, Tibet, China

Introduction: The Abunabu antimony mining area is located between the Indus–Yarlung Tsangpo suture and the southern Tibetan detachment system. Ore deposits in the mining area provide an excellent opportunity to understand the nature and genesis of antimony mineralisation in the Tethys Himalayan metallogenic belt.

Methods: In this study, we analysed the He–Ar and S isotopic compositions of stibnite-hosted fluid inclusions as a basis for investigating the sources of ore-forming fluids in the Abunabu mining area and the Tethys Himalayan metallogenic belt.

Results: The analysed stibnites have ⁴He contents of 0.016 × 10⁻⁷–1.584 × 10⁻⁷ cm³ STP/g, ⁴⁰Ar contents of 1.37 × 10⁻⁷–2.94 × 10⁻⁷ cm³ STP/g, ⁴⁰Ar/³⁶Ar ratios of 303.8–320.7, and ³He/⁴He (Ra) ratios of 0.021–0.351. These isotopic features indicate that the ore-forming fluids were primarily metamorphic fluids of crustal origin, with small amounts of magmatic-derived materials and modified air-saturated water with low ⁴⁰Ar*/⁴He ratios. The δ³⁴S values of stibnite vary within a narrow range of –4.9‰ to –3.5‰, with a mean value of –4.31‰, indicating a deep magmatic origin.

Discussion: On the basis of these results and a compilation of data for sulphide deposits in the metallogenic belt, we infer that compositional variations in the He and Ar isotopes of the ore-forming fluids of each antimony deposit in the Tethys Himalayan metallogenic belt are independent of each other. This suggests that antimony deposits in the belt had similar ore-forming fluid sources and mixing processes and that differences in the metallogenic tectonic setting within the belt emerged only in the later stages of deposit evolution. Our new results and compiled data also show that antimony–gold deposits and lead–zinc–antimony polymetallic deposits in the Tethys Himalayan metallogenic belt differ in their sulphur isotopic compositions and that multiple sulphur sources were involved in each of these types of deposit.

KEYWORDS

source of ore-forming fluid, metallogenic phase, Tethys Himalaya, Abunabu antimony mining area, He-Ar-S isotopes

1 Introduction

The Tethys Himalayan lead–zinc–antimony polymetallic metallogenic belt is located in southern Tibet and consists of various types of Cenozoic polymetallic deposit, such as antimony, antimony–gold, gold, lead–zinc, and lead–zinc–antimony deposits. Major deposits include the Cheqiongzhubu antimony, Abunabu antimony, Mazhala antimony–gold, Chapula gold, Jisong lead–zinc, and Zhaxikang lead–zinc–antimony polymetallic deposits (Yang et al., 2006; 2009; Zheng et al., 2014; Sun et al., 2016; Sun et al., 2018; Zhai et al., 2018; Cao et al., 2019; Wang et al., 2020; Zhang et al., 2021). Although no copper or molybdenum deposits have been discovered in this metallogenic belt, rare-metal (such as tungsten, tin, beryllium, and rubidium) ore deposits have been discovered (Li et al., 2017; Liang et al., 2018; Cao et al., 2021). The Tethys Himalayan metallogenic belt has attracted broad scientific interest, and numerous studies have focused on the ore-forming geological features, ore-controlling factors, metallogenic material sources, metallogenic epochs, and ore-forming processes of antimony–(gold) and lead–zinc deposits (Nie et al., 2005; Hou et al., 2006; Yang et al., 2006; Qi et al., 2008; Zheng et al., 2012; Zhai et al., 2014; Duan et al., 2016; Wang et al., 2017; Xie et al., 2017; Liang et al., 2018; Sun et al., 2018). Some previous studies have established the properties and sources of ore-forming fluids in the antimony deposits (Meng et al., 2008; Yang et al., 2009; Zhu et al., 2012; Xie et al., 2017). Investigation of ore-forming fluids is crucial to the study of hydrothermal ore deposits because these fluids can be used to determine the type of ore deposit, establish the genesis of ore deposits, and guide exploration (Guo et al., 2011). Previous studies have investigated ore deposits in the Longzi–Cuona–Cuomei–Jiangzi area in the eastern Tethys Himalayan metallogenic belt (Wen et al., 2006; Yang et al., 2006; Zhu et al., 2012; Xie et al., 2017; Wang, 2019a; Wang, 2019b; Liang, 2019; Wang et al., 2021). However, the genesis of the antimony, gold, antimony–gold, and lead–zinc–antimony polymetallic deposits in the central and western parts of this metallogenic belt remains poorly understood and continues to be debated (Nie et al., 2005; Yang et al., 2006; Yang et al., 2009; Kali et al., 2010; Hou and Zhang, 2015; Xie et al., 2017). One of the major topics of debate is the classification of the genetic type of the antimony–gold deposits in the belt, with proposals including hydrothermal-vein (Duan et al., 2016), exhalation sedimentation–hydrothermal reformation (Zheng et al., 2014), epithermal cryogenic hydrothermal (Qi et al., 2008) and orogenic (Zhai et al., 2014; Zhai et al., 2018) types.

The Abunabu antimony mining area is located in the western Tethys Himalayan metallogenic belt, approximately 164 km southeast of Shiquanhe Town, Gar County, in the Ali area of Tibet Autonomous Region. Earlier exploration campaigns have revealed that this is a large-scale antimony mining area, with a resource of more than 100,000 t at 4.93% antimony (Fang et al., 2006; Chen et al., 2011). Hence, studying the genesis of the ore deposits in the Abunabu mining area is of significance for revealing the nature and evolution of antimony mineralisation in the Tethys Himalayan metallogenic belt. In this paper, we report the results of detailed field geological and microscope mineralogical investigations and He–Ar–S isotopic geochemical analyses of the Hamuqu and Quzhen antimony deposits in the Abunabu mining area. In addition, we conduct a comparison with the He–Ar–S isotopic compositions of typical antimony deposits in the Tethys Himalayan metallogenic belt to clarify the sources of ore-forming fluids and metals.

2 Regional geological setting

The Himalaya–Tibetan orogen is a tectonic assemblage of five W–E-trending terranes: (from north to south), the Songpan–Ganzi, North Qiangtang, South Qiangtang, Lhasa, and Himalayan terranes. The Himalayan terrane is separated from the Lhasa Block by the Indus–Yarlung Tsangpo suture (IYTS) and from the Indian plate by the Main Frontal Thrust (Figure 1A; e.g.; Yin and Harrison, 2000; Zhang et al., 2004; 2007; Zhang, Zhang, et al., 2012; Cao et al., 2018; Dai et al., 2020; Pan et al., 2022; Ma et al., 2022). The Himalayan terrane is divided (from north to south) into the Tethys Himalayan sequence (THS), the Greater Himalayan Crystalline Complex (GHC), the Lesser Himalayan sequence (LHS), and the sub-Himalayan sequence (SHS), which are separated by the southern Tibet detachment system (STDS), the Main Central Thrust fault (MCT), and the Main Boundary Thrust fault (MBT), respectively (Burchfiel et al., 1992; Yin, 2006; Martin, 2017). Phanerozoic strata exposed in the THS have been deposited on the Indian passive continental margin (Cao et al., 2018; Cao et al., 2020) and comprise mainly Palaeozoic to Palaeogene, low-grade-metamorphic, siliceous clastic and carbonate rocks (Myrow et al., 2019). A series of north Himalayan gneiss domes are developed in the centre of the THS (Cao et al., 2021). Previous studies have suggested that the Neo-Tethyan Ocean opened before the Late Triassic (ca. 230 Ma; Cao et al., 2018) and that oceanic crust began to subduct north-eastward beneath the Lhasa terrane during the Triassic (Wang et al., 2016; Cao et al., 2018; Cao et al., 2020). Rift-related basalts and turbidites of the Langjiexue Group are exposed in the Himalayan region (Cao et al., 2018; 2021; Huang et al., 2018). During the Late Jurassic to Early Cretaceous, the Cuomei igneous province formed, and the Indian plate started to drift northwards from the Australian plate (Zhu et al., 2009; Olierook et al., 2019). During the Jurassic–Cretaceous, numerous marine clastic and carbonate rocks were deposited in the passive continental margin of India. These strata are important host rocks of Pb–Zn–Ag–Sb–Au deposits in the Himalayan region (Yang et al., 2009). Neo-Tethyan oceanic crust was completely subducted beneath the Lhasa plate, and intercontinental collision occurred between the Indian and Lhasa plates during the Cenozoic (55 ± 5 Ma; Hu et al., 2016; Searle, 2019), followed by the subduction of the Indian continental crust (Cao et al., 2021).

In detail, the Himalayan terrane is divided into four major tectonic units (Cao et al., 2018; Figure 1B), which (from north to south) are as follows: (1) The THS, consisting of lower Palaeozoic to Eocene clastic and carbonate rocks deposited on the northern Indian passive margin; (2) the GHC, composed of a Proterozoic to Palaeozoic upper-amphibolite- to granulite-facies metasedimentary sequence (Kohn, 2014); (3) the LHS, including a Proterozoic greenschist- to amphibolite-facies metasedimentary sequence (Richards et al., 2005; Kohn, 2014); and (4) the SHS (Neogene Siwalik Formation), comprising Miocene–Pliocene foreland basin deposits. These four tectonic domains are separated by five boundary systems; i.e., the IYTS, STDS, MCT, MBT, and MFT (Figure 1B; Guillot et al., 2008; Cao et al., 2018). Within the Himalayan terrane, two sub-parallel belts of Cenozoic leucogranites have been identified: the Tethys Himalayan leucogranite belt (also termed the north Himalayan granite) to the north and the High Himalayan leucogranite belt to the south (Figure 1B; Wu et al., 2015; Cao et al., 2022). Intrusions with evident silicification, sericitisation, and carbonatisation have a close

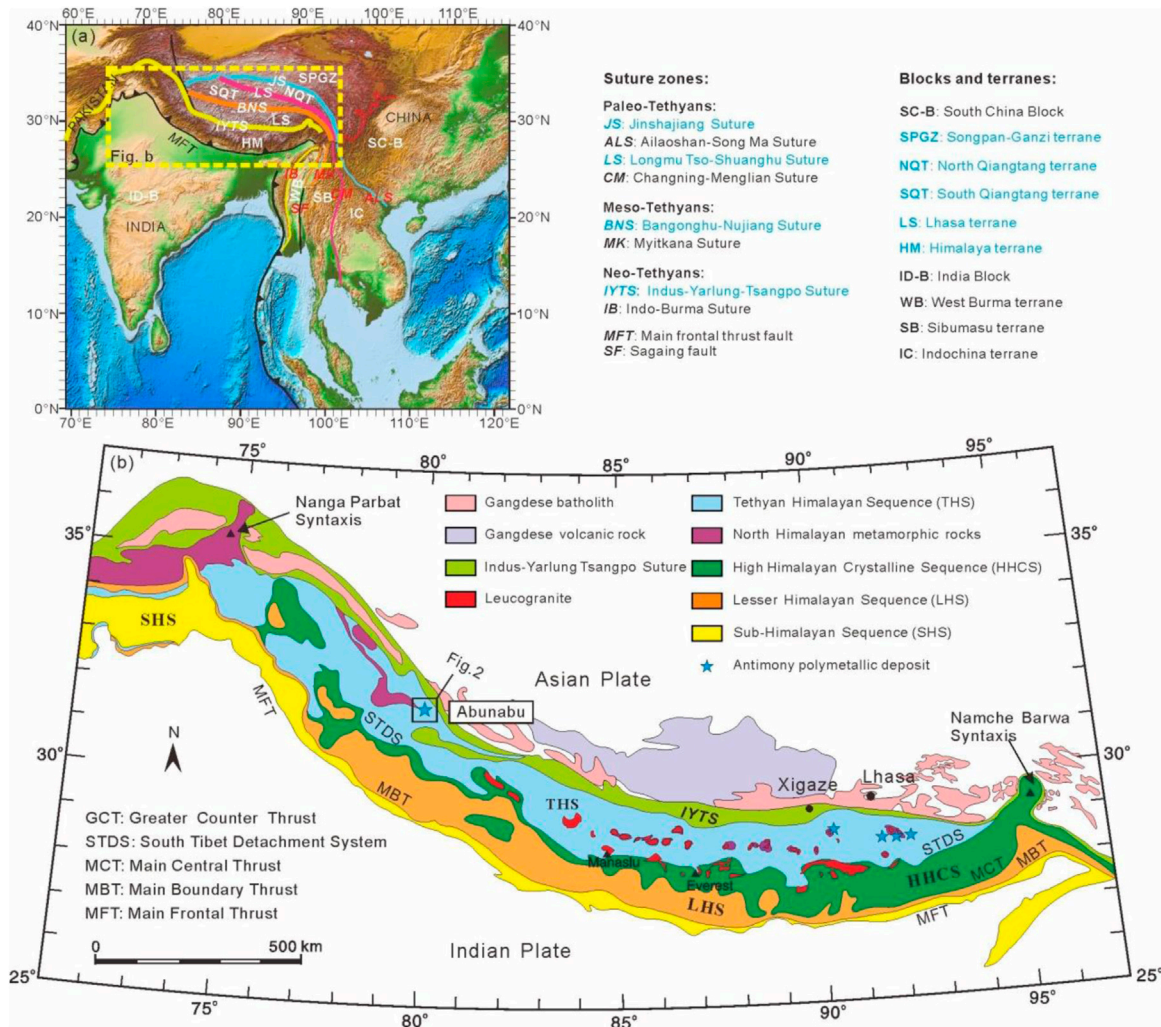


FIGURE 1 Tectonic map of the Himalaya–Tibetan Plateau region: (A) geotectonic sketch of southeastern Asia (Yin and Harrison, 2000; Cao et al., 2018); (B) simplified geological map of Himalaya, showing the major antimony polymetallic deposit (modified after Cao et al., 2018; Guillot et al., 2008; Zhang et al., 2019; Dai et al., 2020).

spatial relationship with antimony, antimony–gold, and gold deposits (Nie et al., 2005).

In terms of tectonic location, the Abunabu mining area is located in the southern margin of the Yarlung Tsangpo suture belt and the western section of the Tethys Himalayan metallogenic belt. The area contains mainly Silurian–Triassic, Palaeogene, and Quaternary strata (Figure 2). The main ore-bearing horizon is the Triassic Qiongguo Group ($T_{1-2}Q$), which is a set of lower-greenschist-facies metamorphic rock series with strong deformation. The primary lithology consists of slate, meta-sandstone (meta-conglomerate), and limestone, with mostly deep-sea turbidite deposits (Zhang et al., 2005).

The Late Cretaceous mélangé (K_2mlg) is a tectonic–lithostratigraphic unit that is sporadically distributed as fragments and blocks. The exposed Nizha mélangé (K_2nmlg) and Boku mélangé (K_2bmlg) are material components of the ophiolite and mélangé in the centre of the NW syncline in the western section of the Yarlung Tsangpo suture zone and together are also known as the

northern tectonic mélangé of the Brahmaputra junction. Magmatic rocks are distributed in the mining and surrounding areas and include Late Cretaceous Banguori lherzolite ($K_2b\phi\sigma$), porphyritic quartz monzodiorite ($K_2\pi\eta\delta\sigma$), and belugite ($K_2\delta\nu$). Medium–fine-grained ($E_2zx\eta\eta$) and medium–coarse-grained ($E_2cz\eta\eta$) monzogranites represent the products of plate subduction–collision events during the Mesozoic–Cenozoic evolution of the Tethyan tectonic regime (Zhang et al., 2005).

3 Ore deposit geology

The Hamuqu and Quzhen deposits (from old to new) are preserved in the Lower–Middle Triassic Qiongguo Group ($T_{1-2}Q$), the Palaeogene Liuqu Group ($E_{1-2}Lq$), and Quaternary strata (Figures 3A,B). Of these, the Quzhen deposit is hosted in Early Cretaceous ultramafic rocks ($K_1\Sigma$) and Late Cretaceous gabbros ($K_2\nu$) (Fang et al., 2006; Chen et al., 2011).

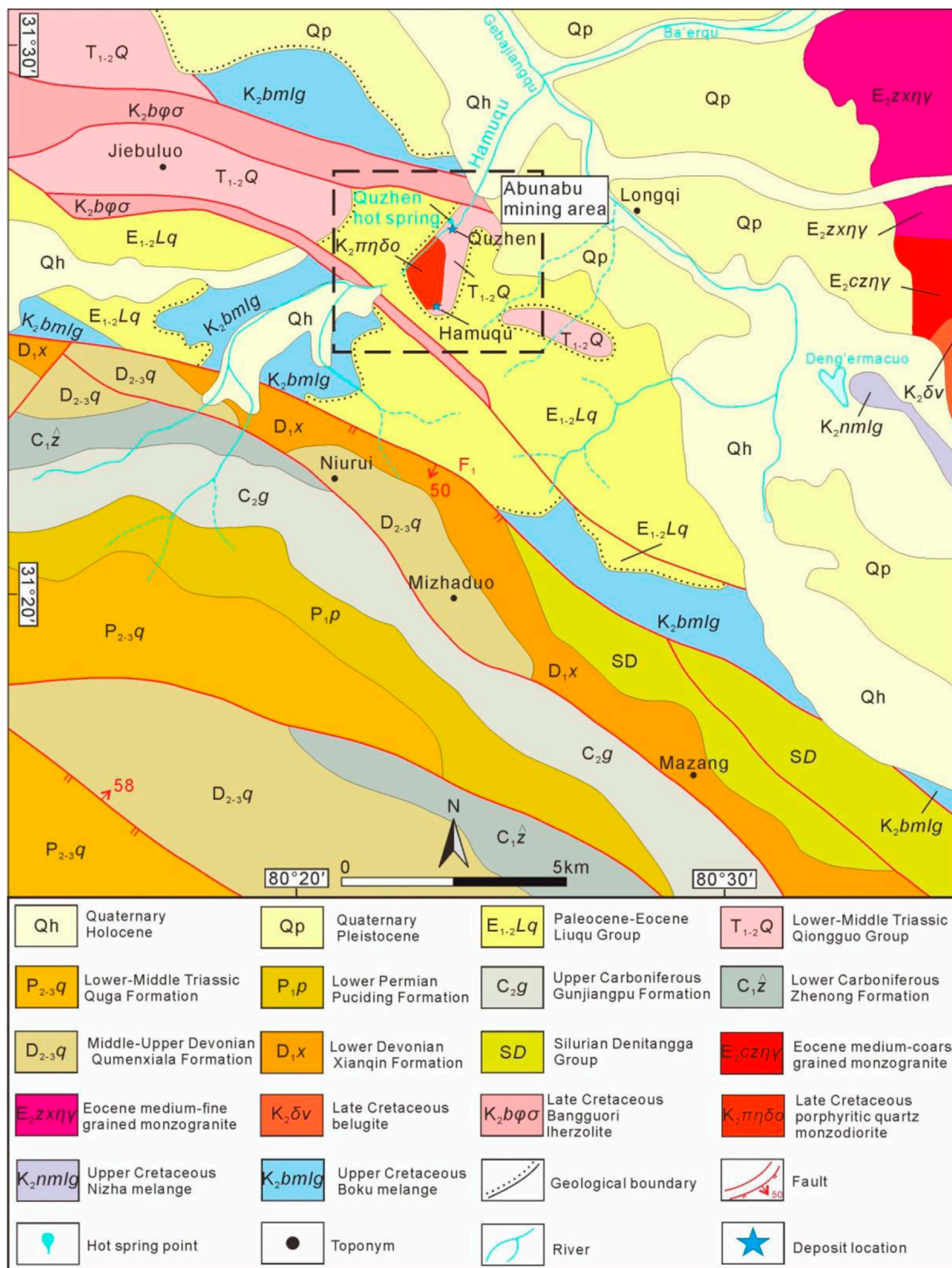
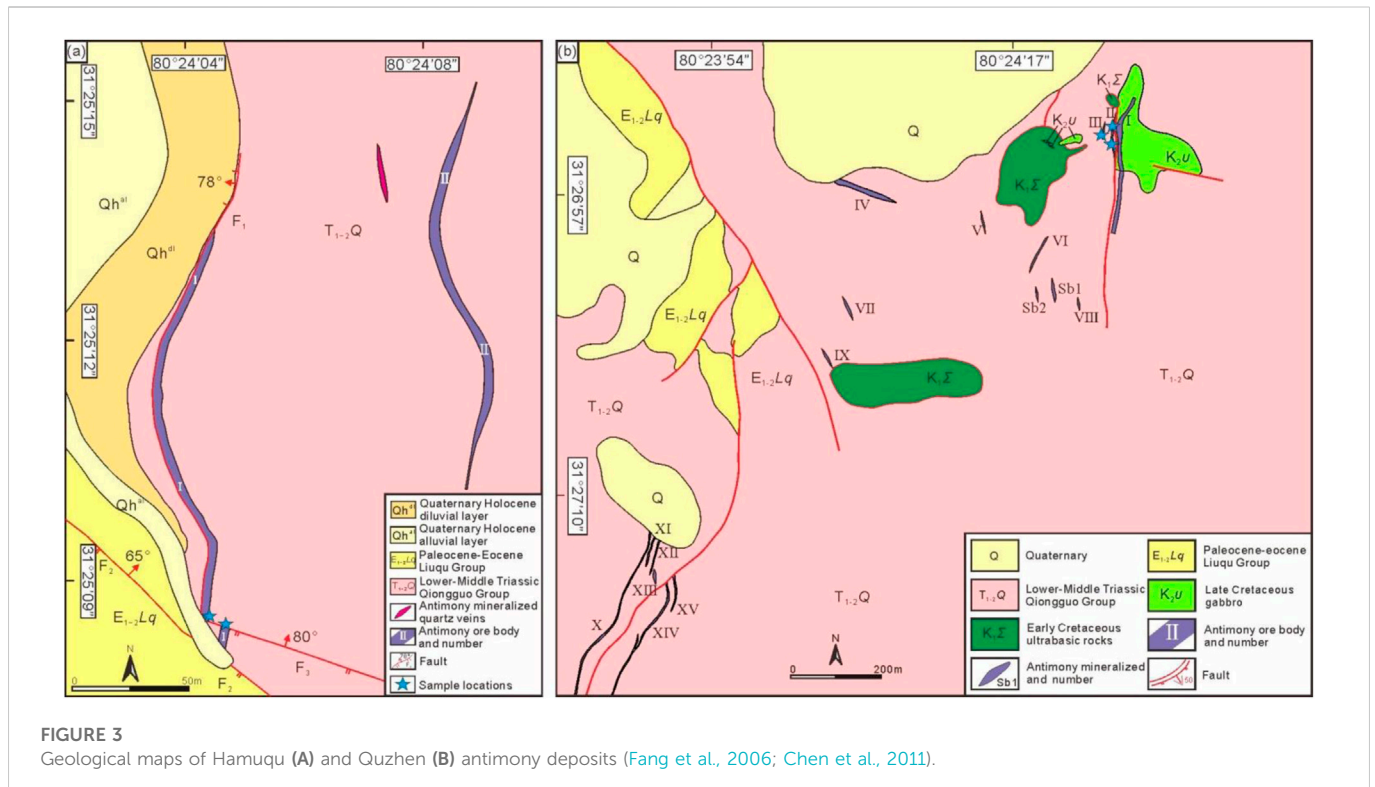


FIGURE 2 Regional geological map of Abunabu antimony ore concentration area (Zhang et al., 2005).

3.1 Hamuqu ore deposit

Two orebodies have been discovered in the Hamuqu antimony deposit. The mineralised alteration zone is formed in the Lower–Middle Triassic Qiongguo Group (T₁₋₂Q), which is a low-metamorphic-grade rock series composed of sericite slate and sericite

siliceous slate. The No. I orebody is strictly controlled by the structure (faults) and is generally distributed along the NNE direction, with a steep dip angle of 65°–80° (Figure 4A). The No. II orebody is located to the northeast of the No. I orebody and is controlled by a NNE-trending pre-mineralisation fault; the wall-rock is Lower–Middle Triassic Qiongguo Group slate (Figure 3A). This orebody generally



strikes NNE and is inclined WNW, with a dip angle of approximately 70°. The antimony orebodies of the Hamuqu deposit are mostly veined, bead-like, and lenticular. The ore minerals are primarily stibnite, with minor pyrite and arsenopyrite, whereas the gangue minerals are mainly quartz and sericite. The ore structure is dominated by columnar, columnar mosaic, and fragmentation and crush structures, appearing mostly in the form of crystal clusters, veinlet dissemination, agglomerates, and sparse dissemination (Figures 4C–F). Wall-rock alteration is dominated by silicification and sericitisation, with minor pyritisation. Stibnite mineralisation is closely related to silicification and sericitisation, with sericitisation occurring later than silicification (Fang et al., 2006).

3.2 Quzhen ore deposit

A total of 17 antimony orebodies have been found in the Quzhen deposit. Antimony orebodies I–II are developed primarily near Late Cretaceous altered gabbro (K_2v) plutons (Figure 4B), extending southwards to slate sandstone of the Lower–Middle Triassic Qiongguo Group ($T_{1-2}Q$). Antimony orebodies III–XV and Sb1–Sb2 occur in slate sandstone of the Lower–Middle Triassic Qiongguo Group ($T_{1-2}Q$) (Figure 3B). The antimony orebodies are mostly layered, veined and lenticular. The ore minerals are predominately stibnite, with minor pyrite, arsenopyrite, and valentinite; the gangue minerals are mainly quartz, muscovite, sericite, and chlorite. Stibnite crystals are primarily euhedral and subhedral, and some display fragmentation and metasomatic textures. Stibnite commonly occurs as granular aggregates with long columnar, radial, veinlet-disseminated, sparsely disseminated, crystal-cluster, and dense lumpy structures. Wall-rock alteration types are mainly silicification, carbonatisation, sericitisation, and

pyritisation (Figures 4G–J). Silicification has generated numerous quartz veins and is closely related to mineralisation, as stibnite occurs mainly in zones of strong silicification (commonly containing quartz veins; Chen et al., 2011).

3.3 Stages of mineralisation in the abunabu deposits

Three stages of mineralisation can be identified in the deposits in the Abunabu mining area: (1) sedimentary metamorphic stage, (2) hydrothermal stage, and (3) supergene stage (Figure 5).

During the sedimentary metamorphic stage, sericite-, sericite–silica-, and sericite–silt-altered slates underwent regional dynamic metamorphism after undergoing regional N–S faulting and the formation of tectonic breccia. Sericite, muscovite, chlorite, and fine-grained quartz were generated by metamorphism of slate, without stibnite.

The hydrothermal stage was affected by regional extensional structures; early fault structures were reactivated, and numerous N–S-trending fault structures were formed. Deep ore-forming hydrothermal fluid ascended into shallow parts along fault structures and migrated into fault zones and the surrounding rocks. Multi-stage hydrothermal activity resulted in the alteration and mineralisation of slate, tectonic breccia, and magmatic rocks. Three different types of quartz formed during this stage and are spatially associated with large amounts of stibnite and quartz–sulphides and minor pyrite, arsenopyrite, and calcite.

Finally, in the supergene stage, after the hydrothermal stage and strong weathering, valentinite formed in orebodies at the surface. Simultaneously, some native sulphur formed as a result of hot spring activity.

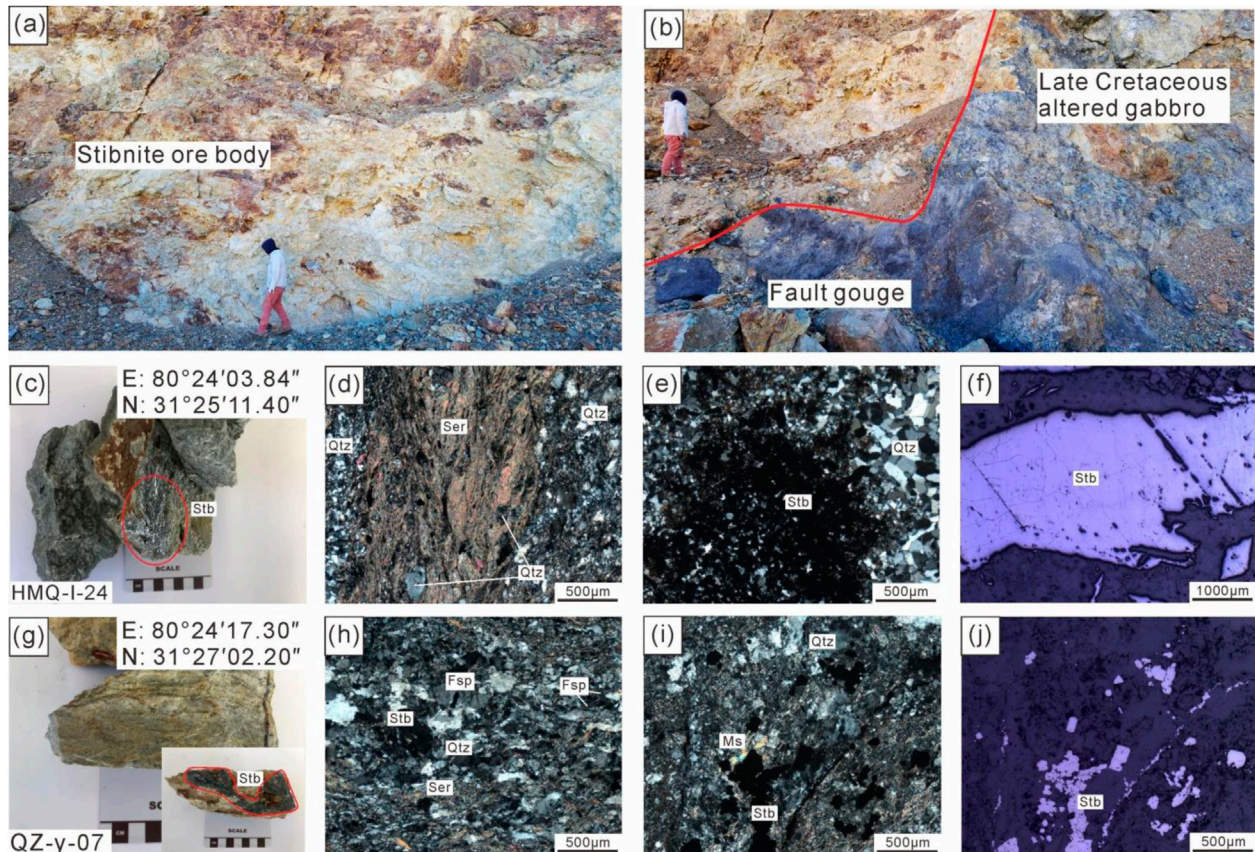


FIGURE 4

Field, hand specimens and microscopic photos of the Hamqu and Quzhen antimony de-posits (A): field photo of Hamuqu I orebody; (B) field photo of Quzhen I orebody, the orebody is in contact with the fault zone and the late Cretaceous altered gabbro (K_2v); (C–F): hand specimens and microscopic photographs of dark gray sericite silty slate in the Hamuqu deposit; (G–J): hand specimens and microscopic photographs of greyish-green phyllitization sericeous slate in the Quzhen deposit; Qtz: quartz; Ser: sericite; Ms: muscovite; Fsp: feldspar; Stb: stibnite).

3.4 Controls on metallogenesis

Regional geological data and detailed field observations show that the strata most closely spatially associated with antimony mineralisation in the Abunabu deposits are the Middle–Upper Devonian Qumexiala Formation (D_{2-3q}) and the Lower–Middle Triassic Qiongguo Group (T_{1-2Q}). Intrusive rocks exposed in the Quzhen deposit, which is located in the northern part of the mining area, are mostly Early Cretaceous ultramafic rocks ($K_1\Sigma$) and Late Cretaceous gabbros (K_2v). The mineralisation in this area is closely spatially related to the distribution and type of sedimentary strata, structures, and magmatic rocks, as follows (Chen et al., 2011).

- 1) Sedimentary strata. Strata including those of the Qumexiala Formation (D_{2-3q}) and the Qiongguo Group (T_{1-2Q}) are found in the mining area. The orebodies are hosted mainly in certain rock types, including crystalline limestone, sericite slate, and meta-sandstone. The spatial distributions of the orebodies are thus associated with the distributions of particular stratigraphic units.
- 2) Structure. Well-developed fault structures occur in the mining area, such as NW–SE-trending and near-N–S-trending faults, which control the directional distribution of the orebodies.

- 3) Magmatic rocks. In the Quzhen deposit, some of the main metallogenic sites are found in the inner and outer contact zones between Early Cretaceous ultramafic rocks ($K_1\Sigma$) and Late Cretaceous gabbro (K_2v) and the Qiongguo Group (T_{1-2Q}) strata (Figure 3B). In general, magmatic rocks are expected to provide large amounts of gas, hydrothermal fluids, metals, and thermal energy for mineralisation and play a key role in the activation, migration, and enrichment of metallogenic elements.

4 Genetic mechanism of the ore deposits

4.1 Samples and analytical method

In this study, nine samples from fresh stibnite ores obtained from the Hamuqu and Quzhen deposits in the Abunabu antimony mining area were analysed for He, Ar, and S isotopes. Sample lithologies and sampling locations are given in Table 1. To characterize the mineralogy, textures, and mineral paragenesis of these samples, polished blocks and thin sections were examined by reflected and transmitted light microscopy.

Stage Mineral	Sedimentary metamorphic	Hydrothermal	Supergene
Quartz	■ ■ ■	■ ■ ■	
Muscovite	■ ■ ■		
Sericite	■ ■ ■		
Chlorite	■		
Stibnite		■ ■ ■	
Pyrite		■	
Calcite		■	
Arsenopyrite		■	
Native sulphur			■
Valentinite			■ ■ ■
■ ■ ■ Major ■ ■ Minor ■ Trace minerals			

FIGURE 5

The metallogenic phase division and mineral paragenetic sequence of the Abunabu antimony deposits (Fang et al., 2006; Chen et al., 2011).

The He and Ar isotopic compositions of stibnite fluid inclusions were analysed at the Key Laboratory of Mineralisation and Resource Evaluation, Ministry of Natural Resources, Institute of Mineral Resources, Chinese Academy of Geological Sciences, Beijing, China, using a Helix SFT noble gas mass spectrometer. The setup consists of crushing, purification, and mass spectrometry systems. Analyses were performed under high-vacuum conditions, namely, $n \times 10^{-9}$ mbar for the crushing and purification system, and $n \times 10^{-10}$ mbar for the mass spectrometer system. A Nier-type ion source was used in the mass spectrometer, and the sensitivity was better than 2×10^{-4} amps/Torr for He under a trap current of 800 μ A and better than 1×10^{-3} amps/Torr for Ar under a trap current of 200 μ A. The static rise rate of ^{40}Ar was less than 1×10^{-12} cm^3 SPT/min, and the background value of ^{36}Ar was less than 5×10^{-14} cm^3 SPT. A Faraday cup resolution of >400 and an ion counter resolution of >700 allowed complete separation of the ^3He and ^4He , HD + H_3 , and ^3He peaks. The procedure involved the following steps for each sample: (1) A high-purity 40–60 mesh sample was washed and dried. An amount of 0.5–1.0 g of the sample was placed in a stainless-steel crucible; the crucible was sealed, heated for degassing, and vacuumed. (2) The sample was crushed, inclusion gases were purified in multiple stages, and pure He and Ar were separated. (3) Testing of isotope composition of He and Ar was

performed. (4) Isotope ratio results were corrected using test results of the air standard of the day and the air standard value. The standard value of $^3\text{He}/^4\text{He}$ in air is 1.4×10^{-6} , and the standard values of $^{40}\text{Ar}/^{36}\text{Ar}$ and $^{36}\text{Ar}/^{38}\text{Ar}$ are 295.5 and 5.35, respectively. (5) The ^4He and ^{40}Ar contents (cm^3 SPT/g) of the samples were evaluated using 0.1 ml standard gas ^4He (52.3×10^{-8} cm^3 SPT/g) and ^{40}Ar (4.472×10^{-8} cm^3 SPT/g); the isotopic signal intensity of the standard gas and the sample and the mass of the crushed and sieved (below 100 mesh) sample were used to calibrate the sample ^4He and ^{40}Ar contents (Li, et al., 2015).

Sulphur isotope analysis was conducted at the Isotope Laboratory of the Institute of Mineral Resources, Chinese Academy of Geological Sciences, using a MAT-251 mass spectrometer for analysis with Vienna Canyon Diablo Troilite (VCDT) as the standard. The specific procedure was as follows. First, single mineral specimens of stibnite were manually selected under a binocular microscope, with a purity of >95%. Subsequently, the selected specimens were ground to less than 200 mesh in an agate bowl, and a specific proportion of CuO was added. The mixture was mixed well and put in a container, which was placed into a muffle furnace. The reaction was performed at 1000°C for 15 min in a vacuum, during which sulphur in the minerals was oxidised to SO_2 , which was collected and analysed for isotope composition. The analytical accuracy was $\pm 0.2\%$ (Brian et al., 2002).

TABLE 1 Location and brief descriptions of the samples used for He–Ar–S isotopes analysis.

Mining area	Sample no.	Sample locations	Analytical mineral	Lithology	Paragenetic association of minerals	Petrographic description
Hamuqu	HMQ-I-24	Near the F ₃ fault in the No. I orebody	Stibnite	Dark grey sericite silty slate	Quartz–stibnite–sericite–feldspar	The rock has a silty texture, lepidoblastic texture and plate structure. Mainly quartz and sericite, with a small amount of feldspar and muscovite. The quartz is mostly of a variable grain shape and has the characteristics of tensile orientation distribution as a whole. Sericites are arranged in parallel and oriented microscales. A small amount of mica, mixed in sheets with sericite, is the main result of sericite alteration. The feldspar is scattered in the rocks in a plate shape, and clays occur commonly
	HMQ-I-25		Stibnite		Quartz–stibnite–sericite–feldspar–muscovite	
	HMQ-I-28		Stibnite		Quartz–stibnite–sericite–feldspar–muscovite	
Quzhen	QZ-Y-7	The No. III orebody	Stibnite	Greyish-green phyllitisation sericeous slate	Quartz–stibnite–sericite–feldspar–muscovite	The rock is light grey-green, with a dense, massive structure and a lepidoblastic texture. The main mineral compositions are sericite and quartz, among which sericite is scaly and fibrous, with the directional or semi-directional arrangement. It is a shallow metamorphic product of argillaceous rock
	QZ-Y-23		Stibnite		Quartz–stibnite–sericite–feldspar–muscovite	
	QZ-Y-13	The contact of No. II ore body with faults and gabbro	Stibnite	Dark grey sericite silty slate	Quartz–stibnite–sericite–feldspar	The rock has a silty texture, lepidoblastic texture and plate structure. Mainly quartz and sericite, with a small amount of feldspar. The quartz is mostly of a variable grain shape and has the characteristics of tensile orientation distribution as a whole. Sericites are arranged in parallel and oriented microscales. The feldspar is scattered in the rocks in a plate shape, and clays occur commonly
	QZ-Y-15		Stibnite		Quartz–stibnite–sericite–feldspar	
	QZ-Y-16		Stibnite		Quartz–stibnite–sericite–feldspar	
	QZ-Y-17		Stibnite		Quartz–stibnite–sericite–feldspar	

5 Results

The analytical results for He–Ar–S isotopes of stibnite from the Hamuqu and Quzhen deposits in the Abunabu mining area are listed in Table 2 and Supplementary Table S3. Stibnite is the most important ore mineral in the study area and the main sulphide mineral, meaning that its fluid inclusions should be the best record of the original information of the ore-forming fluids of the metallogenic period. The ⁴He contents of stibnite in the Hamuqu antimony deposit are 1.057×10^{-7} – 1.584×10^{-7} cm³ STP/g, and the ⁴⁰Ar contents are 1.37×10^{-7} – 2.48×10^{-7} cm³ STP/g. In addition, ⁴⁰Ar/³⁶Ar ratios vary widely between 303.8 and 320.7. Furthermore, ³He/⁴He (Ra) ratios range from 0.021 to 0.031. In stibnite from the Quzhen antimony deposit, the He signals of samples QZ-Y-13, QZ-Y-15, QZ-Y-16, and QZ-Y-17 samples were weak, and ⁴He contents vary widely from 0.016×10^{-7} to 0.772×10^{-7} cm³ STP/g. The ⁴⁰Ar contents are 1.40×10^{-7} – 2.94×10^{-7} cm³ STP/g, and ⁴⁰Ar/³⁶Ar ratios lie between 295.6 and 302.2. The ³He/⁴He (Ra) ratios have larger values of 0.025–0.351

(Table 2). As shown in Figure 6, there is a good correlation between the He and Ar isotopic compositions of the analysed fluid inclusions.

The δ³⁴S values of stibnite from the Hamuqu deposit in the Abunabu antimony mining area range from –4.9‰ to –4.4‰, with a mean of –4.7‰, whereas the δ³⁴S values of antimonite in the Quzhen deposit lie between –4.9‰ and –3.5‰, with a mean of –4.1‰ (Supplementary Table S3). The variation in sulphur isotope composition of the nine stibnite samples is narrow, indicating that the Hamuqu and Quzhen deposits shared a common or similar source of sulphur.

6 Discussion

6.1 Source of the ore-forming fluids

Isotopes of He and Ar have been widely used to determine the origin of ore-forming fluids (Hu et al., 1999; Ballentine and Burnard,

TABLE 2 He and Ar isotopic compositions of fluid inclusions of typical antimony polymetallic deposits in the Tethys Himalaya metallogenic belt.

Location	Sample number	Mineral	⁴ He	⁴⁰ Ar	³ He/ ³⁶ Ar	³ He/ ⁴ He	⁴⁰ Ar*	³ He/ ⁴ He	⁴⁰ Ar/ ³⁶ Ar	⁴⁰ Ar*	⁴ He/ ³⁶ Ar	F ₄ He	Mantle derived He%	⁴⁰ Ar*/ ⁴ He	R/Ra	References	
			(10 ⁻⁷ cm ³ STP/g)						(Ra)	(%)							
Mazhala	09MZL-2-12	stibnite	48	7.12	2206.161	0.790	2.042	0.056	414.3	28.675	2793.034	16876.337	0.562	0.043	0.040	Zhai et al. (2018)	
	09MZL-1-5	stibnite	99.3	6.35	40947.547	0.549	5.957	0.039	4770.1	93.805	74593.847	450718.110	0.296	0.060	0.028		
	09MZL-1-7	stibnite	133.3	10.52	6055.692	0.604	6.591	0.043	791.3	62.656	10026.644	60583.949	0.357	0.049	0.031		
	09MZL-1-8a	stibnite	69.7	2.33	2007.206	0.193	0.345	0.014	346.8	14.792	10374.232	62684.180	–	0.005	0.010		
	09MZL-1-15	stibnite	42	4.21	1775.450	0.464	0.968	0.033	383.7	22.987	3827.886	23129.220	0.203	0.023	0.024		
	2010121	stibnite	63.1	3.52	2337.142	0.434	0.060	0.031	300.6	1.697	5388.597	32559.496	0.169	0.001	0.022		
	2010129	quartz	786	75.1	15674.091	0.557	66.847	0.040	2689.1	89.011	28144.242	170055.845	0.305	0.085	0.028		
	09MZL-1-9	pyrite	233	48.5	2858.856	0.469	37.195	0.034	1267.7	76.690	6090.188	36798.717	0.209	0.160	0.024		
	09MZL-1-14	pyrite	36.4	19.2	687.393	0.780	6.993	0.056	464.8	36.424	881.183	5324.371	0.551	0.192	0.040		
	09MZL-2-2	pyrite	24.7	13.37	790.181	1.224	2.063	0.087	349.4	15.426	645.488	3900.232	1.041	0.084	0.062		
	MZL-1	pyrite	70.2	3.03	20593.390	1.960	1.056	0.140	453.5	34.840	10506.832	63485.388	1.852	0.015	0.100		Zhang, (2012)
	MZL-3	pyrite	118.4	8.79	5825.172	1.400	0.381	0.100	308.9	4.338	4160.837	25141.011	1.235	0.003	0.071		
MZL-2	pyrite	300	9.58	19791.733	1.540	2.682	0.110	410.4	27.997	12851.775	77654.227	1.389	0.009	0.079			
Shalagang	09SL-1-7	stibnite	52.6	12.01	1468.884	0.685	39.645	0.049	489.6	39.645	2144.293	12956.454	0.446	0.091	0.035	Zhai et al. (2018)	
	09SL-1-8	stibnite	49.6	8.51	1207.858	0.422	39.792	0.030	490.8	39.792	2860.597	17284.574	0.157	0.068	0.022		
	09SL-1-10	stibnite	22.5	6.16	1378.259	0.813	36.356	0.058	464.3	36.356	1695.901	10247.136	0.587	0.100	0.041		
	09SL-7-2	stibnite	13.45	9.19	1040.167	1.608	33.130	0.115	441.9	33.130	646.742	3907.804	1.464	0.226	0.082		
	09SL-8-2	stibnite	114.2	11.09	3066.859	0.664	34.158	0.047	448.8	34.158	4621.547	27924.757	0.423	0.033	0.034		
	09SL-8-5	stibnite	89.4	9.4	1598.598	0.334	41.299	0.024	503.4	41.299	4787.655	28928.431	0.059	0.043	0.017		
	09SL-8-7	stibnite	146	16.9	2349.028	0.504	45.227	0.036	539.5	45.227	4660.769	28161.748	0.247	0.052	0.026		
	2010098	stibnite	18.9	6.22	758.743	0.569	32.719	0.041	439.2	32.719	1334.547	8063.726	0.318	0.108	0.029		
	2010105	stibnite	10.73	4.12	531.831	0.599	13.292	0.043	340.8	13.292	887.569	5362.954	0.352	0.051	0.031		
Zhaxikang	ZXKPD7-8e	sphalerite	39	2.46	100347.476	0.63	2.388	0.045	10047.0	97.059	159281.707	962427.235	0.386	0.061	0.032	Zhang, et al. (2010)	
	ZXKPD7-8f	siderite	55.8	15	1906.987	1.106	5.437	0.079	463.5	36.246	1724.220	10418.248	0.910	0.097	0.056		
	ZXKPD6-1c	quartz	1.49	29.7	176.811	2.408	23.704	0.172	1463.6	79.810	73.426	443.664	2.346	15.908	0.123		
	ZXKPD6-2c	quartz	1.89	27.7	239.472	2.366	22.182	0.169	1483.4	80.080	101.214	611.565	2.299	11.737	0.121		

(Continued on following page)

TABLE 2 (Continued) He and Ar isotopic compositions of fluid inclusions of typical antimony polymetallic deposits in the Tethys Himalaya metallogenic belt.

Location	Sample number	Mineral	⁴ He	⁴⁰ Ar	³ He/ ³⁶ Ar	³ He/ ⁴ He	⁴⁰ Ar*	³ He/ ⁴ He	⁴⁰ Ar/ ³⁶ Ar	⁴⁰ Ar*	⁴ He/ ³⁶ Ar	F ₄ He	Mantle derived He%	⁴⁰ Ar*/ ⁴ He	R/Ra	References
			(10 ⁻⁷ cm ³ STP/g)						(Ra)	(%)	(%)					
	ZXKPD5-6d	stibnite	0.2	3.49	–	0.574	–	0.041	–	–	–	–	0.324	–	0.029	Zhang, (2012)
	ZXKPD5-6e	quartz	0.09	32.6	1.543	0.672	21.015	0.048	831.5	64.462	2.296	13.870	0.432	233.495	0.034	
	ZXKPD5-8c	quartz	15.2	18	14798.538	18.270	12.455	1.305	959.2	69.193	809.991	4894.206	19.830	0.819	0.932	
	ZXK-1	pyrite	31.2	4.05	1340.814	0.560	0.199	0.040	310.8	4.923	2394.311	14467.137	0.309	0.006	0.029	
	ZXK-2	pyrite	12.57	1.74	1168.750	0.560	-	0.040	288.9	-	2087.053	12610.595	0.309	–	0.029	
	ZXK-3	pyrite	21	2.68	1394.087	0.560	0.187	0.040	317.7	6.988	2489.440	15041.935	0.309	0.009	0.029	
Abunabu	HMQ-I-24	stibnite	1.584	2.48	60.212	0.310	0.070	0.022	304.1	2.828	194.232	1173.605	0.031	0.044	0.016	This study
	HMQ-I-25	stibnite	1.057	1.88	75.155	0.440	0.051	0.031	303.8	2.732	170.807	1032.065	0.170	0.049	0.022	
	HMQ-I-28	stibnite	1.058	1.37	74.299	0.300	0.108	0.021	320.7	7.858	247.665	1496.463	0.015	0.102	0.015	
	QZ-Y-5-7	stibnite	0.723	1.75	43.698	0.350	0.039	0.025	302.2	2.217	124.852	754.391	0.077	0.054	0.018	
	QZ-Y-23	stibnite	0.772	1.4	61.555	0.370	0.029	0.026	301.7	2.055	166.366	1005.233	0.093	0.037	0.019	
	QZ-Y-13	stibnite	0.053	1.7	13.277	1.430	0.013	0.102	297.8	0.772	9.284	56.099	1.265	0.248	0.073	
	QZ-Y-15	stibnite	0.025	2.66	8.835	3.180	0.001	0.227	295.6	0.034	2.778	16.787	3.194	0.036	0.162	
	QZ-Y-16	stibnite	0.017	2.94	7.215	4.190	0.023	0.299	297.8	0.772	1.722	10.405	4.306	1.336	0.214	
	QZ-Y-17	stibnite	0.016	2.54	9.208	4.910	0.019	0.351	297.7	0.739	1.875	11.331	5.108	1.173	0.251	

STP indicates the standard temperature and pressure state.

⁴⁰Ar* represents the relative content of radiogenic.

⁴⁰Ar in the ore-forming fluids; $n(^{40}\text{Ar}^*) = n(^{40}\text{Ar})_{\text{Sample}} - 295.5 \times n(^{36}\text{Ar})_{\text{Sample}}$; the F₄He value represents the amount of.

⁴He in the fluids relative to air; $F_4\text{He} = [n(^4\text{He})/n(^{36}\text{Ar})]_{\text{Sample}} / [n(^4\text{He})/n(^{36}\text{Ar})]_{\text{Air}}$, $[n(^4\text{He})/n(^{36}\text{Ar})]_{\text{Air}} = 0.1655$.

⁴He_{Mantle} represents the proportion of mantle source He, $n(^4\text{He})_{\text{Mantle}} = 100\% \times \{ [n(^3\text{He})/n(^4\text{He})]_{\text{Sample}} - [n(^3\text{He})/n(^4\text{He})]_{\text{Crustal}} \} / \{ [n(^3\text{He})/n(^4\text{He})]_{\text{Mantle}} - [n(^3\text{He})/n(^4\text{He})]_{\text{Crustal}} \}$, $[n(^3\text{He})/n(^4\text{He})]_{\text{Mantle}} = 6.5\text{Ra}$, $[n(^3\text{He})/n(^4\text{He})]_{\text{Crustal}} = 0.02\text{Ra}$, $\text{Ra} = [n(^3\text{He})/n(^4\text{He})]_{\text{Air}} = 1.4 \times 10^{-6}$ (Stuart et al., 1995; Anderson, 2000).

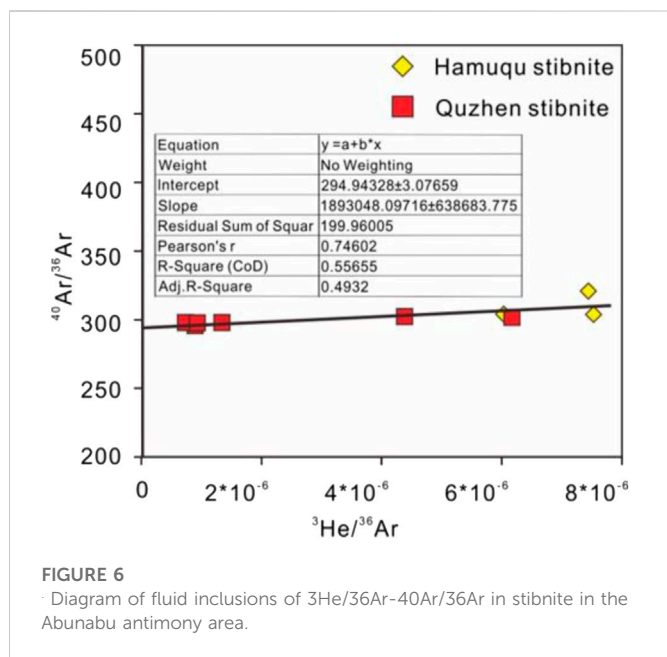


FIGURE 6
Diagram of fluid inclusions of $^3\text{He}/^{36}\text{Ar}$ - $^{40}\text{Ar}/^{36}\text{Ar}$ in stibnite in the Abunabu antimony area.

2002). The gases He and Ar are present in minerals in three main forms: (1) in fluid inclusions that are captured by minerals; (2) radioactive ^4He and ^{40}Ar resulting from the decay of U, Th, and K in the mineral lattice; and (3) He and Ar from the atmosphere adsorbed onto mineral surfaces (Burnard et al., 1999). However, He and Ar in sulphides of hydrothermal deposits are found predominantly in mineral fluid inclusions (Turner and Stuart, 1992; Stuart et al., 1995). Owing to the low contents of U, Th, K, and other lithophile elements in fluid inclusions in the sulphide minerals of non-uranium deposits (with Th being almost insoluble in hydrothermal fluids), and because fluid inclusions in sulphide minerals are surrounded after closure, the presence of radiogenic He and Ar formed by the decay of U, Th, and K was considered negligible in the present study (Turner and Wang, 1992; Qiu, 1996; Burnard and Poly, 2004; Hu et al., 2004; 2012; Ding et al., 2014).

The content of He in the atmosphere is minimal and insufficient to substantially affect the content and isotopic composition of He in crustal fluids (Marty et al., 1989; Stuart et al., 1994; Hu et al., 2009). If a sample contains atmospheric He, then $F^4\text{He}$ should be equal to 1 (Kendrick et al., 2001; Mao and Li, 2004). As presented in Table 2, the $F^4\text{He}$ values of stibnite in the Abunabu antimony ore area range

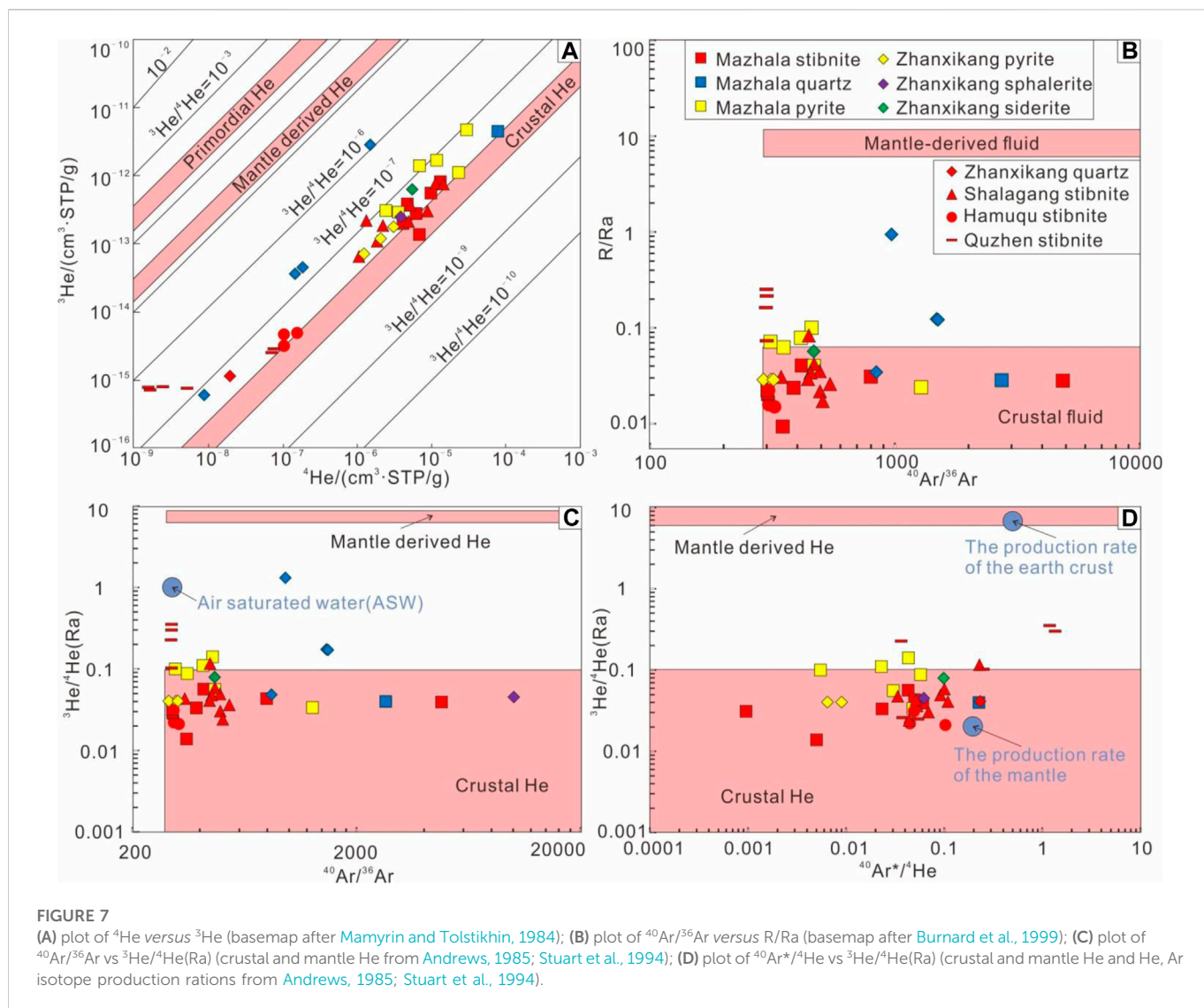


FIGURE 7
(A) plot of ^4He versus ^3He (basemap after Mamyrin and Tolstikhin, 1984); (B) plot of $^{40}\text{Ar}/^{36}\text{Ar}$ versus R/Ra (basemap after Burnard et al., 1999); (C) plot of $^{40}\text{Ar}/^{36}\text{Ar}$ vs $^3\text{He}/^4\text{He}(Ra)$ (crustal and mantle He from Andrews, 1985; Stuart et al., 1994); (D) plot of $^{40}\text{Ar}^*/^4\text{He}$ vs $^3\text{He}/^4\text{He}(Ra)$ (crustal and mantle He and He, Ar isotope production ratios from Andrews, 1985; Stuart et al., 1994).

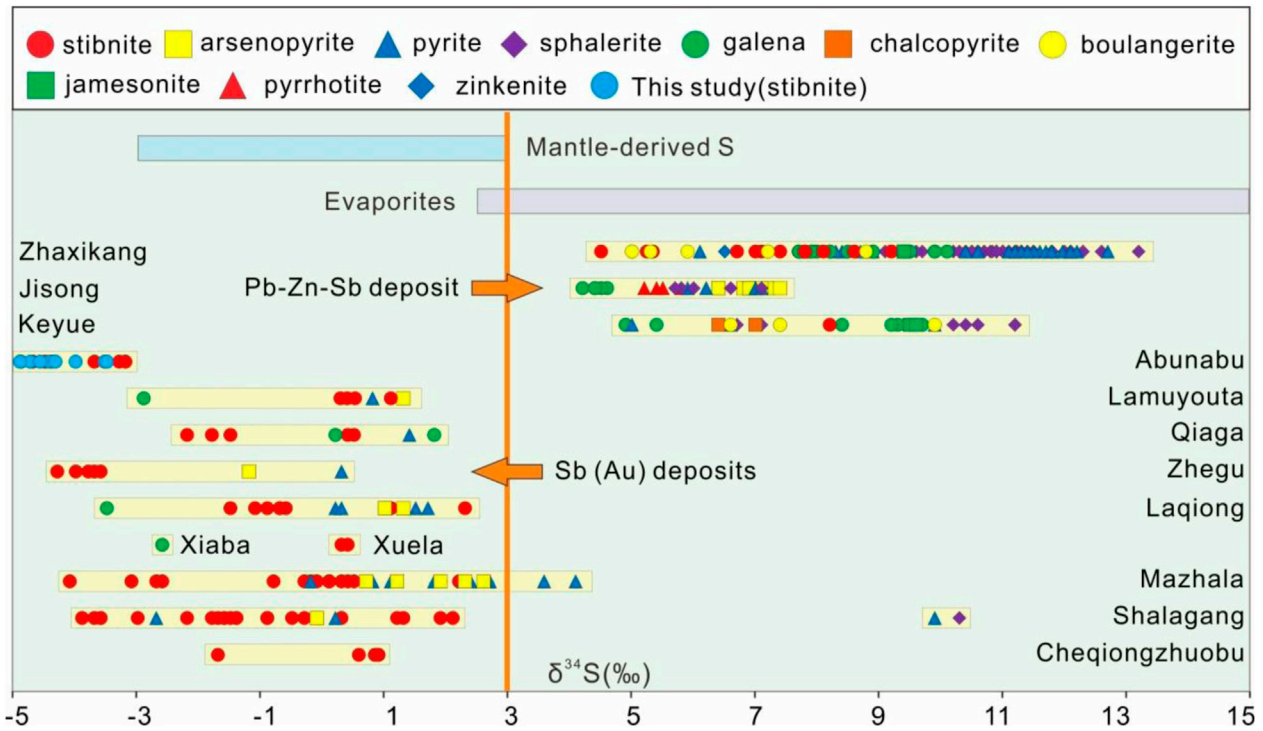


FIGURE 8 Sulphur isotopic composition of typical antimony polymetallic deposits in the Tethys Himalaya metallogenic belt [comparison of the S isotope composition derived from the mantle, and evaporites (Heyl et al., 1974; Zou et al., 2017; 2019; Cao et al., 2019)].

between 10.40 and 1,496.46, all greater than 1, suggesting no atmospheric He. Isotope data for He and Ar in this study were obtained from inclusions in stibnite, which should represent the initial values of the primary fluid inclusions. Owing to the unique nature of noble gases, no significant isotopic fractionation occurs whether the fluid inclusion samples are collected during mineralisation or obtained by crushing in a vacuum (Hu et al., 1999). Hu et al. (1999) studied the He–Ar isotopic geochemistry of ore-forming fluids of the Ailaoshan gold deposits and found that when fluid inclusions in chalcopyrite, galena, stibnite, and other minerals are diffused in large quantities to lose He, no obvious fractionation is observed in the He isotopes, meaning that the measured $^3\text{He}/^4\text{He}$ and $^{40}\text{Ar}/^{36}\text{Ar}$ ratios represent the initial values of the ore-forming fluids when the fluid inclusions were captured.

Noble gases have distinct He and Ar isotopic compositions in the atmosphere and crustal and mantle rocks. Thus, these gases are widely used to trace the source of ore-forming fluids. Isotopes of He and Ar in hydrothermal fluids are derived largely from the following sources (Burnard et al., 1999; Ballentine and Burnard, 2002), (1) The atmosphere or atmospheric saturated water (e.g., meteoric, sea, or sedimentary water). The atmosphere has a stable He–Ar isotopic composition, with $^3\text{He}/^4\text{He} = 1.399 \times 10^{-6}$ and $^{40}\text{Ar}/^{36}\text{Ar} = 295.5$. Atmospheric saturated water is in equilibrium with the atmosphere under certain temperature and pressure conditions and has a similar isotopic composition to that of the atmosphere. Because the He content in air is low and its solubility in aqueous solution is the lowest of the noble gases, the He content in saturated atmospheric water is low ($\text{He}/\text{Ar} \approx 1 \times 10^{-4}$; Simmons et al., 1987; Burnard et al., 1999). Due to the relatively high content of Ar in the

atmosphere, the closure temperature of Ar in rocks is far higher than that of He (McDougall et al., 1988). Therefore, shallow groundwater contains almost no radioactive Ar but has characteristics consistent with the isotopic composition of atmospheric Ar. The radioactive-origin ^4He generated by the decay of U and Th in aquifer rocks diffuses into groundwater or geothermal fluids, the $^3\text{He}/^4\text{He}$ ratio of geological fluids derived from atmospheric water or seawater is lower than its atmospheric value, and the ^4He content of geological fluids is higher than that of atmospheric saturated water. Therefore, shallow groundwater or near-surface cryogenic fluids have lower $^3\text{He}/^4\text{He}$ ratios than those in the atmosphere and $^{40}\text{Ar}/^{36}\text{Ar}$ ratios that are similar to atmospheric values, indicating the characteristics of modified air-saturated water (Ballentine and Burnard, 2002). (2) Mantle-derived fluids. The $^3\text{He}/^4\text{He}$ ratio of fluids from the continental lithospheric mantle is in the range of six to eight Ra (where Ra is the atmospheric value), whereas that of oceanic lithospheric mantle fluids is in the range of six to nine Ra (Gautheron and Moreira, 2002). Mantle-derived Ar is mainly $^{40}\text{Ar}^*$ of radioactive origin, and the $^{40}\text{Ar}/^{36}\text{Ar}$ ratio varies considerably and is usually greater than 40,000 (Porcelli et al., 1992; Patterson et al., 1994; Reid and Graham, 1996). Because of the very large difference in the $^3\text{He}/^4\text{He}$ ratio between crust and mantle, even if there is a small amount of mantle He mixed in crustal fluids, this component can be easily identified using He isotopes (Simmons et al., 1987; Stuart et al., 1995; Hu et al., 1999). (3) Crustal fluids. Owing to the high content of large-ion lithophile elements in crustal rocks, the radioactive and nucleogenic He and Ar produced by these elements are characterised by a $^{40}\text{Ar}/^{36}\text{Ar}$ ratio of ≥ 295.5 and a $^3\text{He}/^4\text{He}$ ratio

of 0.01–0.05 Ra (Andrews and Lee, 1979; Stuart et al., 1995), such that metamorphic or magmatic fluids of crustal origin show similar He and Ar isotopic compositions to those of crustal rocks.

Data for a total of 41 analysed samples from four antimony deposits (Abunabu, Mazhala, Shalagang, and Zhaxikang) in the Tethys Himalayan metallogenic belt were compiled from this study and previous studies (Table 2). For these 41 analysed samples, the $^3\text{He}/^4\text{He}$ values of stibnite, pyrite, sphalerite, siderite, and quartz ranged from 0.014 to 1.305 Ra, with a mean of 0.105 Ra. Of these samples, the values for two stibnite samples (QZ-Y-7 and QZ-Y-23) from the Abunabu deposits fall within the crustal $^3\text{He}/^4\text{He}$ value range (0.01–0.05 Ra), whereas the remaining stibnite samples from the Quzhen deposit all display high $^3\text{He}/^4\text{He}$ values that are characteristic of the crust and lower $^3\text{He}/^4\text{He}$ values in the mantle range (six to nine Ra) (Stuart et al., 1995). The former values indicate that the He isotopes in the ore-forming fluids are of crustal origin; the latter values suggest that the He isotopes in the ore-forming fluids are a mixture of mantle and crustal origins. In an He isotopic composition distribution map (Figure 7A), the data points all fall in the transition zone between mantle-derived and crust-derived He, but they tend more towards the crust than the mantle. These data give estimated proportions of mantle-derived fluids in the stibnite samples from the Hamuqu and Quzhen deposits of 0.015%–0.169% (with a mean of 0.065%) and 0.077%–5.108% (with a mean of 2.341%), respectively. Regionally, one quartz sample from the Zhaxikang lead–zinc–antimony polymetallic deposit shows a proportion of mantle-derived fluids of 19.830%, whereas the proportion of mantle-derived fluids in samples from other deposits is less than 3% (Zhang et al., 2010). These results indicate that mantle-derived fluids made an overall minimal contribution to mineralisation and instead suggest a predominant crustal origin for the ore-forming fluids of antimony deposits in the Tethys Himalayan metallogenic belt. The involvement of mantle-derived fluids may be due to the water–rock reaction between the ore-forming fluid and the intermediate–basic magmatic rocks in the region, which activated part of the ore-forming materials such as Sb and Au. (Deng, 2020; Sun et al., 2020).

The $^{40}\text{Ar}/^{36}\text{Ar}$ ratios of the analysed fluid inclusions in stibnite from the Abunabu mining area range from 295.6 to 320.7, with a mean of 302.4, which is slightly higher than the characteristic value of $^{40}\text{Ar}/^{36}\text{Ar}$ in saturated atmospheric water (295.5) but substantially lower than that in the mantle ($^{40}\text{Ar}/^{36}\text{Ar} > 40,000$). Using least squares regression ($^{40}\text{Ar}/^{36}\text{Ar} = 294.94 + 1,893,048.09 \times ^3\text{He}/^{36}\text{Ar}$) to fit the stibnite sample data in Figure 6, when $^3\text{He}/^{36}\text{Ar} = 5 \times 10^{-8}$ (the $^3\text{He}/^{36}\text{Ar}$ value of rainwater), $^{40}\text{Ar}/^{36}\text{Ar} \approx 295.03$, which is within error of the isotopic composition of atmospheric argon ($^{40}\text{Ar}/^{36}\text{Ar} \approx 295.5$). Moreover, this result is consistent with a considerably small amount of excess argon, which implies that the ore-forming fluids of the antimony deposits in the Abunabu mining area constitute a crustal end-member with the input of atmospheric precipitation (Hu et al., 1999; Chen et al., 2016).

A projection of the He and Ar isotopic compositions measured in this study onto a R/Ra– $^{40}\text{Ar}/^{36}\text{Ar}$ diagram (Figure 7B) shows that the compositions are distributed in the crustal fluid field or between crustal and mantle fluids (and closer to crustal fluids). Furthermore, the $^{40}\text{Ar}/^{36}\text{Ar}$ isotope ratios of all samples from the Abunabu mining area are greater than the atmospheric $^{40}\text{Ar}/^{36}\text{Ar}$ isotope ratio, implying the presence of crust-derived radiogenic Ar ($^{40}\text{Ar}^*/\%$) in the fluids. Calculations show that the proportion of

radiogenic Ar in Abunabu mining area is in the range of 0.772%–7.858%, which indicates that only a low content of radiogenic Ar ($^{40}\text{Ar}^*/\%$) originated from the crust. Due to the different degrees of greenschist facies metamorphism of the host strata, the source of ore-forming fluid is also the result of the joint action of the modified air-saturated water and metamorphic fluid (Zhai et al., 2018; Li H et al., 2022). In comparison, Figure 7C shows that a few samples lie close to the atmospheric saturated water field, suggesting that in addition to crustal fluids, mantle-derived fluids and a small amount of atmospheric precipitation were involved in the mineralisation. Therefore, the antimony deposits in the Tethys Himalayan metallogenic belt display the characteristics of mixed mineralisation involving modified air-saturated water rich in atmospheric argon, crustal fluids containing He, and crustal fluids containing radioactively derived Ar.

The lithospheric mantle has $^{40}\text{Ar}^*/^4\text{He} = 0.5$ and $^3\text{He}/^4\text{He} =$ six to nine Ra, and crustal rocks have values of $^{40}\text{Ar}^*/^4\text{He} = 0.2$ and $^3\text{He}/^4\text{He} < 0.1$ Ra (Andrews, 1985). $^{40}\text{Ar}^*/^4\text{He}$ values in the Hamuqu and Quzhen deposits are 0.0443–0.1018 and 0.0360–1.3357, respectively. Excluding the two samples whose values are higher than the mantle average in the Quzhen deposit (1.336 and 1.173), the rest fall substantially below the crustal mean. On a $^{40}\text{Ar}^*/^4\text{He}$ – $^3\text{He}/^4\text{He}$ map (Figure 7D), most sample data for antimony deposits in the Tethys Himalayan metallogenic belt plot in the crustal source area. Furthermore, $^{40}\text{Ar}^*/^4\text{He}$ ratios lie between the average end-member of the crustal rock yield and the end-member of the crustal rock yield. Previous studies have also found that in the antimony deposits of the Tethys Himalayan metallogenic belt (such as the Shalagang Sb deposit and Mazhala Sb–Au deposit), as well as the involvement of metamorphic fluids of crustal origin, there was addition of modified air-saturated water with low $^{40}\text{Ar}^*/^4\text{He}$ (Zhang, 2012; Zhai et al., 2018; Li et al., 2021; Liu et al., 2021). It is consistent with the results of hydrogen and oxygen isotope analysis, the ore-forming fluid is mainly composed of meteoric water and the addition of metamorphic fluid (Zhai et al., 2014).

Sphalerite, siderite, and pyrite from the Zhaxikang deposit have similar $^3\text{He}/^4\text{He}$ and $^{40}\text{Ar}/^{36}\text{Ar}$ values, which represent the characteristics of fluids during the early metallogenic stage. In an R/Ra– $^{40}\text{Ar}/^{36}\text{Ar}$ diagram, sphalerite, pyrite, and siderite all lie in the range of crustal fluids (Figure 7B). The He–Ar isotopic characteristics of quartz fluid inclusions in stibnite vein ores differ from those of the early zinc–lead ore-forming fluids, indicating the influence of mantle-derived fluids. Therefore, the ore-forming fluids of the early lead–zinc ore in the Zhaxikang deposit are composed mainly of crust-derived fluids, whereas the ore-forming fluids of the late stibnite are composed predominantly of mantle-derived fluids, which also suggests that the early ore-forming fluids of this deposit may have been seafloor hot brine (Zhang, 2016). Moreover, all data points for the particular same deposit are distributed parallel to the Y-coordinate axis (Figure 7C), implying that the variation in He isotopes in the ore-forming fluids was largely unaffected by Ar. Therefore, in the Tethys Himalayan metallogenic belt, the compositional variations in He and Ar isotopes in the ore-forming fluids of each antimony deposit are independent of each other. This result suggests that antimony deposits in the belt had similar fluid sources and mixing processes and that differences in the metallogenic tectonic setting within the belt emerged only in the later stages of evolution of the deposit.

6.2 Source of the ore-forming materials

Sulphur is an important metal transportation agent for ore-forming hydrothermal fluids and can therefore be used to infer the source of ore-forming materials (Li et al., 2020a; Li et al., 2021). The heavy S isotope, ^{34}S , tends to fractionate to sulphate relative to sulphide; however, under reducing environments, sulphide is the predominant S phase, meaning that ^{34}S values can approximately represent the bulk S isotopic composition (Ohmoto, 1972; Seal, 2006; Li et al., 2020b).

No sulphate minerals are found in the Hamuqu and Quzhen deposits of the Abunabu mining area, suggesting a reducing environment of formation, and the main sulphur-bearing mineral assemblages are sulphides such as stibnite, arsenopyrite, and pyrite. Therefore, the S isotopic compositions of the stibnite samples analysed in the present study are considered to represent the bulk S isotopic composition of the Abunabu mining area. The mean $\delta^{34}\text{S}$ value of stibnite in the Hamuqu and Quzhen deposits is -4.7‰ , within the range of $\delta^{34}\text{S}$ values of antimonite in the Quzhen deposit of -4.9‰ to -3.5‰ (mean value of -4.1‰) and slightly lower than typical magmatic sulphur $\delta^{34}\text{S}$ values (-3‰ to $+3\text{‰}$; Chaussidon et al., 1989). The source of sulphur may have been mainly deep magmatic sulphur (Yang et al., 2009; Li et al., 2018; 2019; Cao et al., 2019; Li C L et al., 2022), with the slightly lower values reflecting the possible addition of small amounts of minerogenetic materials from the Qiongguo Group ($T_{1-2}Q$). Numerous intermediate–mafic dikes occur in the Abunabu mining area, and the Late Cretaceous gabbro body (K_2v) is the ore-bearing protolith of the No. I antimony orebody of the Quzhen deposit (Figure 3B), the mineralisation of which evidently occurred later than the intrusion of the intermediate–mafic dikes. Moreover, the intermediate–mafic dikes display alteration, suggesting that sulphur was not directly released by magma but may have been leached from the intermediate–mafic dikes during interaction between hydrothermal fluids and rocks.

A compilation of S isotope data (Supplementary Table 3) for sulphides from typical deposits in the Tethys Himalayan metallogenic belt is presented in Figure 8. The S isotopic compositions of the antimony–(gold) deposits and lead–zinc–antimony polymetallic deposits in this metallogenic belt allow the deposits to be divided into two categories (Figure 8). The first category includes antimony–(gold) deposits such as the Abunabu, Shalagang, Laqiong, Lamuyouta, and Cheqiongzhubu deposits. The range of sulphide $\delta^{34}\text{S}$ for this category is relatively narrow, from -4.9‰ to -4.1‰ , apart from two anomalously high $\delta^{34}\text{S}$ values for pyrite and sphalerite from the Shalagang deposit of 9.9‰ and 10.3‰ , respectively, which are in marked contrast to the $\delta^{34}\text{S}$ values of sulphides from various deposits in the western Tethys Himalayan metallogenic belt, and are not discussed here. The $\delta^{34}\text{S}$ values of sulphides in these deposits are similar to those of skarn-type (-3.9‰ to -0.9‰) and porphyry-type (-1.7‰ to $+2.1\text{‰}$) deposits in Tibet (Zhou et al., 2017), suggesting that deep magma was the main source of sulphur for all of these deposits (Cao et al., 2019; Deng et al., 2019; Li B. L et al., 2022). In addition, the $\delta^{34}\text{S}$ values of antimony and gold deposits in the Tethys Himalayan metallogenic belt are similar to those in the Gangdese porphyry copper belt in Tibet (-6.3‰ to $+1.8\text{‰}$; Qu and Li, 2002), implying that the metallogenesis of antimony–(gold) in this metallogenic belt might be genetically related to large-scale leucogranite magmatism in southern Tibet (Zhou et al., 2017).

The second category of deposits is represented by lead–zinc–antimony polymetallic deposits such as Zhaxikang and Keyue, where sulphide $\delta^{34}\text{S}$ values vary from four‰ to 13‰, close to the $\delta^{34}\text{S}$ values (4.9‰–11.5‰) of the Ridang Formation; i.e., the main ore-bearing horizon in the study area (Zheng et al., 2003; Zhang, 2012). These deposits may contain sulphur that was derived from rocks deposited in a marine environment, and such sulphur was likely strongly involved in the mineralisation of Zhaxikang, Keyue, and other lead–zinc–antimony polymetallic deposits (Zhou et al., 2017; Sun et al., 2018). In summary, the two categories of deposits in the Tethys Himalayan metallogenic belt classified in terms of their sulphide $\delta^{34}\text{S}$ values had multiple sources of sulphur (Deng et al., 2019; Li et al., 2020b).

Although antimony–(gold) deposits and lead–zinc–antimony polymetallic deposits in the Tethys Himalayan metallogenic belt may have had the same sources of metal elements (deep metamorphic crystalline basement and leucogranite), the sources of sulphur of the associated ore-forming fluids differed considerably between these two types of deposit. Fluids of the former deposits were derived primarily from the magmatic system, whereas those of the latter deposits were derived predominantly from the surrounding black sedimentary rock series. In terms of the compositions of metallogenic elements, those deposits with magma-derived sulphur—including Abunabu—are dominated by antimony or antimony–gold mineralisation, whereas the element combination involved in sedimentary metallisation is mostly lead–zinc mineralisation, with antimony produced principally as associated ore. Therefore, sulphur isotopic compositions can be used to identify deposit types and give prospecting guidance for ore types in the Tethys Himalayan metallogenic belt (Du et al., 2011; Li et al., 2021).

6.3 Genesis of mineral deposits in the Tethys Himalayan metallogenic belt

Antimony deposits in southern Tibet have undergone three major stages of mineralisation (Fan et al., 2012; Li et al., 2014; Deng et al., 2019): the source bed formation stage, the preliminary mineral enrichment stage, and the superimposed mineral enrichment stage. The formation stage of the initial source beds occurred during the Late Triassic to Early Cretaceous, coinciding with the formation and development stage of the Neo-Tethys Ocean. In addition to rifting, the thick turbidite sedimentary structure that formed during this period laid the material foundation for mineralisation in southern Tibet. This structure included basalt-dominated magmatic rocks and hydrothermal sedimentary rocks. During the preliminary enrichment stage of minerals by dynamic hydrothermal metamorphism during the Late Cretaceous–Oligocene, the Indian plate subducted northwards beneath Asia, and the Tibetan Tethys Ocean gradually narrowed and closed, the crust thickened, and intra-continental orogenesis formed folds and thrust-nappe structures, resulting in regional low-temperature dynamic metamorphism. Subsequently, owing to the detachment of lithospheric mantle, mantle heat flow ascended, accompanied by granite emplacement and regional heat flow metamorphism, resulting in the extraction of H_2O , CO_2 , Cl, S, Sb, As, Au, and other elements from the ore bearing formation-tectonic, thereby forming ore-bearing fluids. Under the influence of a temperature and pressure gradient, these fluids migrated and

precipitated minerals in the low-pressure dilatant zone, resulting in mineral enrichment (Li H et al., 2022). During the tectonic–magmatic superimposed enrichment mineralisation stage, which occurred after the Miocene, the Indian plate continued to subduct northwards, resulting in lateral extrusion and NE–SW-directed tensile stress. A series of near-N–S-trending high-angle normal faults were formed together with the emplacement of deep mafic magma, and some of these faults continued to develop to form horst–graben structures and faulted basins. This group of fault zones and horst–graben structures connected the magmatic–hydrothermal system with the groundwater hydrothermal system, providing favourable space for the migration and enrichment of ore-bearing hydrothermal solution, forming epithermal antimony–(gold) ore and ‘hot spring type’ antimony ore (Hou et al., 2006; Zhou et al., 2014; Liang, 2019).

Groves et al. (1998) considered that the temperature required for metamorphic fluids to activate Sb elements from surrounding rocks is the temperature corresponding to amphibolite-facies metamorphism. This temperature condition is much higher than that of the metamorphic grade of the rocks surrounding the Abunabu mining area, indicating that regional ore-forming fluids were derived predominantly from magmatic water. However, considering that most of the antimony–gold polymetallic deposits in the Tethys Himalayan metallogenic belt are distributed around metamorphic domes, the possible influence of metamorphic fluids on mineralisation cannot be ignored (Yang et al., 2009). Zheng et al. (2022) proposed that the Sb in antimony deposits of the Tethys Himalayan metallogenic belt was sourced from subvolcanic magmatism which involves rich volatiles formed from decompression and fusion of hypomagma and is responsible for the development of exhalative sedimentation-reworked, magmatic hydrothermal and hot spring deposits.

Although no metamorphic dome has been found near the Abunabu mining area, He–Ar isotope compositions indicate that metamorphic fluids of crustal origin were involved in the mineralisation process. We consider that the temperature of metamorphic fluids in the process of NE-directed tectonic migration decreased with increasing migration distance and was not sufficiently high to activate Sb, Au, and other ore-forming elements in the surrounding rock. Therefore, magmatic–hydrothermal fluids are inferred to have been responsible for the activation of Sb, Au, and other ore-forming elements. The mixing of magmatic fluids and metamorphic fluids involved in the migration of metallogenic materials is dependent on physical and chemical conditions, such as fluid composition, temperature, pressure, and pH. These conditions, together with mixing of atmospheric precipitation, provided favourable conditions for subsequent mineralisation in the Abunabu mining area (Yang et al., 2009; Deng, 2020).

The low $\delta^{34}\text{S}$ values of stibnite from the Abunabu mining area indicate that the ore-forming fluids involved in the mineralisation of the Hamuqu and Quzhen antimony deposits were a mixture of magmatic and metamorphic fluids. Moreover, the proportion of mantle-derived He in the analysed stibnite is less than 3%, implying that although mantle-derived materials were involved in the mineralisation, the degree of influence was much smaller than that of the dominant crustal source, from which the ore-forming fluids were mainly derived. Mafic magmatic rocks such as gabbro and

ultramafic rocks are widely exposed in the regional strata, and the small amount of mantle-derived material in stibnite from the Abunabu mining area may be related to the magma that formed these rocks.

In summary, our analysis of ore-forming fluids and material sources leads us to conclude that the initial ore-forming fluids of the Hamuqu and Quzhen antimony deposits were a mixture of deep magmatic fluids and metamorphic–hydrothermal fluids derived from crust–mantle differentiation. When the magmatic fluids carrying metallogenic materials in the deep crust flowed and ascended into the low-grade-metamorphic sedimentary rocks of the Qiongguo Group ($T_{1-2}Q$) along a regional shear zone, large volumes of metamorphic fluids and extracted metallogenic materials from these sedimentary rocks were added to the magmatic fluids. Finally, the ore minerals were precipitated from these ore-forming fluids along tensional and torsional fracture zones (Liu et al., 2018; Li L et al., 2022).

7 Conclusion

- 1) The Hamuqu and Quzhen deposits in the Abunabu mining area of the Tethys Himalayan metallogenic belt host antimony mineralisation that formed over three stages; i.e., the sedimentary metamorphic, hydrothermal, and supergene stages.
- 2) The He–Ar isotopic characteristics of fluid inclusions in stibnite indicate that the ore-forming fluids of the Hamuqu and Quzhen deposits were predominantly metamorphic fluids of crustal origin and included small proportions of magmatic-derived materials and modified air-saturated water with low $^{40}\text{Ar}^*/^{4}\text{He}$ ratios. Isotope compositional data for sulphides show that antimony deposits in the Tethys Himalayan metallogenic belt had similar fluid sources and mixing processes but that later evolutionary processes differed between the deposits as a result of variations in the metallogenic tectonic environment within the belt.
- 3) The $\delta^{34}\text{S}$ values of stibnite are consistent with magmatic sulphur, suggesting that the sulphur was derived mainly from a deep magmatic source. Analysis of compiled data for sulphide deposits in the Tethys Himalayan metallogenic belt reveals that antimony–(gold) and lead–zinc–antimony polymetallic deposits in the belt differ in their sulphur isotopic compositions and that multiple isotopic sulphur sources were involved in each of these types of deposit in the metallogenic belt.
- 4) Crustal fluids were the main contributors to the ore-forming fluids responsible for the metallogenesis of antimony deposits in the Abunabu mining area.

Data availability statement

The original contributions presented in the study are included in the article/supplementary material, further inquiries can be directed to the corresponding authors.

Author contributions

CW and YL; data curation, YL; writing—original draft preparation, YL; supervision, CW, YL, and YL; project administration, YS, YL, and MP. Funding acquisition, CW, YL, YS,

XZ, GM, and ZY. All authors have read and agreed to the published version of the manuscript.

Funding

This study was funded by “Geology of mineral resources in China” project from China Geological Survey (Grant No. DD20221695, DD20190379, DD20160346) and “Chengdu University of Technology Postgraduate Innovative Cultivation Program: Study on mineralization of the Abunabu antimony deposit in the western section of Tethys Himalayan antimony polymetallic metallogenic belt” (Grant No. CDUT2022BJCX002). The fieldwork was strongly supported by the Tibet Autonomous Region Geological Survey Institute. The experimental content was assisted by researcher Liu Feng and associate researcher Fan Changfu of the Institute of Mineral Resources (IMR), Chinese Academy of Geological Sciences (CAGS). Qin Jinhua, (IMR, CAGS), provided guidance for the revision of the manuscript, and reviewers and the editorial department put forward valuable comments and suggestions, which are hereby acknowledged.

References

- Andrews, J. N., and Lee, D. J. (1979). Inert gases in groundwater from the Bunter Sandstone of England as indicators of age and palaeoclimatic trends. *J. Hydrology* 41 (3–4), 233–252. doi:10.1016/0022-1694(79)90064-7
- Andrews, J. N. (1985). The isotopic composition of radiogenic helium and its use to study groundwater movement in confined aquifers. *Chem. Geol.* 49 (1–3), 339–351. doi:10.1016/0009-2541(85)90166-4
- Awang, J. C., Zheng, Y. Y., Yang, W. T., and Suolang, O. Z. (2017). Mineral typomorphic characteristics and sources of ore forming materials of Keyue lead zinc polymetallic deposit, southern Tibet. *Geol. Sci. Technol. Inf.* 36 (3), 53–63. doi:10.19509/j.cnki.dzqk.2017.0308
- Ballentine, C. J., and Burnard, P. G. (2002). Production, release and transport of noble gases in the continental crust. *Rev. Mineralogy Geochem.* 47 (1), 481–538. doi:10.2138/rmg.2002.47.12
- Brian, Fry., Steven, R. S., Carol, K., and Richard, K. A. (2002). Oxygen isotope corrections for online $\delta^{34}\text{S}$ analysis. *Rapid Commun. Mass Spectrom.* 16 (9), 854–858. doi:10.1002/rcm.651
- Burchfiel, B. C., Chen, Z. L., Hodges, K. V., Liu, Y. P., Royden, L. H., Deng, C. R., et al. (1992). The south Tibetan detachment system, Himalayan orogen: Extension contemporaneous with and parallel to shortening in a collisional mountain belt. *Geol. Soc. Am. Spec. Pap.* 269, 1–41. doi:10.1130/SPE269-p1
- Burnard, P. G., Hu, R. Z., Turner, G., and Bi, X. W. (1999). Mantle, crustal and atmospheric noble gases in Ailaoshan gold deposits, Yunnan Province, China. *Geochimica Cosmochimica Acta* 63 (10), 1595–1604. doi:10.1016/S0016-7037(99)00108-8
- Burnard, P. G., and Polya, D. A. (2004). Importance of mantle derived fluids during granite associated hydrothermal circulation: He and Ar isotopes of ore minerals from Panasqueira 1. Associate editor: R. Wieler. *Geochimica Cosmochimica Acta* 68 (7), 1607–1615. doi:10.1016/j.gca.2003.10.008
- Cao, H. W., Huang, Y., Li, G. M., Zhang, L. K., Wu, J. Y., Dong, L., et al. (2018). Late triassic sedimentary records in the northern tethyan Himalaya: Tectonic link with greater India. *Geosci. Front.* 9 (1), 273–291. doi:10.1016/j.gsf.2017.04.001
- Cao, H. W., Li, G. M., Zhang, L. K., Dong, L., Gao, K., and Dai, Z. W. (2020). Monazite U-Th-Pb age of Liemai Eocene granites in the southern Tibet and its geological implications. *Sediment. Geol. Tethyan Geol.* 40, 31–42. doi:10.19826/j.cnki.1009-3850(2020)02-0031-12
- Cao, H. W., Li, G. M., Zhang, R. Q., Zhang, Y. H., Zhang, L. K., Dai, Z. W., et al. (2021). Genesis of the Cuonadong tin polymetallic deposit in the Tethyan Himalaya: Evidence from geology, geochronology, fluid inclusions and multiple isotopes. *Gondwana Res.* 92, 72–101. doi:10.1016/j.jgr.2020.12.020
- Cao, H. W., Pei, Q. M., Santosh, M., Li, G. M., Zhang, L. K., Zhang, X. F., et al. (2022). Himalayan leucogranites: A review of geochemical and isotopic characteristics, timing of formation, Genesis, and rare metal mineralization. *Earth-Science Rev.* 234, 104229. doi:10.1016/j.earscirev.2022.104229
- Cao, H. W., Zou, H., Bagas, L., Zhang, L. K., Zhang, Z., and Li, Z. Q. (2019). The Laqiong Sb–Au deposit: Implications for polymetallic mineral systems in the Tethys–Himalayan zone of southern Tibet, China. *Gondwana Res.* 72, 83–96. doi:10.1016/j.jgr.2019.02.010
- Chaussidon, M., Albarède, F., and Sheppard, S. M. (1989). Sulphur isotope variations in the mantle from ion microprobe analyses of micro–sulphide inclusions. *Earth Planet. Sci. Lett.* 92 (2), 144–156. doi:10.1016/0012-821X(89)90042-3
- Chen, X., Su, W. C., and Huang, Y. (2016). He and Ar isotope geochemistry of ore-forming fluids for the Qinglong Sb deposit in Guizhou Province, China. *Acta Petrol. Sin.* 32 (11), 3312–3320.
- Chen, Y. M., Da, P. Q., Xiao, N. C., Liu, J. J., Jing, K., Yang, L., et al. (2011). *Detailed investigation report of antimony deposit in Abunabu mine area, gar county, Tibet autonomous region.* Tibet Autonomous Region: Lhasa: Regional Geological Survey Team, Bureau of Geology and Mineral Resources Exploration and Development. (in Chinese).
- Dai, Z. W., Dong, L., Li, G. M., Huizenga, M. J., Ding, J., Zhang, L. K., et al. (2020). Crustal thickening prior to 43 Ma in the Himalaya: Evidence from lower crust–derived adakitic magmatism in Dala, eastern Tethyan Himalaya, Tibet. *Geol. J.* 55, 4021–4046. doi:10.1002/gj.3639
- Deng, Z. (2020). *Study on genesis of the Mazhala Au–Sb deposit in south Tibet (thesis).* Chengdu, China: Chengdu University of Technology. doi:10.26986/d.cnki.gcdlc.2020.000479
- Deng, Z., Zhang, G. Y., Zheng, Y. Y., and Chen, Y. L. (2019). S–Pb isotope constrains for origin of ore forming material in Cheqiongshuobu antimony deposit in southern Tibet. *J. Hefei Univ. Technol. Nat. Sci.* 42 (03), 337–345. doi:10.3969/j.issn.1003-5060.2019.03.007
- Ding, D. J., Liang, J. L., Sun, W. D., Guo, J. H., Li, H., and Ye, X. R. (2014). He–Ar isotopes tracing for ore genesis of the yangshan gold deposit. *Bulletin of mineralogy. Petrology Geochem.* 33 (06), 813–819. doi:10.3969/j.issn.1007-2802.2014.06.009
- Du, Z. Z. (2011). *Geological, geochemical characteristics and genesis of the Lamuyouta Sb (Au) deposit, south Tibet (thesis).* Beijing: China University of Geosciences.
- Du, Z. Z., Gu, X. X., Li, G. Q., Zhang, Y. M., Cheng, W. B., Jing, L. B., et al. (2011). Sulfur, lead isotope composition characteristics and the relevant instructive significance of the Lamuyouta Sb (Au) deposit, south Tibet. *Geoscience* 25 (5), 853–860.
- Duan, J. L., Tang, J. X., and Lin, B. (2016). Zinc and lead isotope signatures of the Zhaxikang Pb–Zn deposit, south Tibet: Implications for the source of the ore-forming metals. *Ore Geol. Rev.* 78, 58–68. doi:10.1016/j.oregeorev.2016.03.019
- Fan, W. Y., Zhu, H. P., Gao, J. H., Yan, J., and Mima, C. R. (2012). Characteristics and Genesis of the Cheqiongshuobu antimony deposit in Tibet. *Mineral. Deposits* 31 (S1), 1019–1020. (in Chinese). doi:10.16111/j.0258-7106.2012.s1.515
- Fang, H. Y., Zou, P. X., Shentu, B. Y., Yu, Q. Z., and Zou, Y. X. (2006). *Antimony deposit, Hamuqu mining area, gaer county, xusong Tibet autonomous region.* Chengdu, China: Chengdu Institute of Geology and Mineral Resources. (in Chinese).
- Groves, D., Goldfarb, R. J., Gebremariam, M., Hagemanna, S. G., and Robertd, F. (1998). Orogenic gold deposits: A proposed classification in the context of their crustal distribution and relationship to other gold deposit types. *Ore Geol. Rev.* 13 (1–5), 7–27. doi:10.1016/S0169-1368(97)00012-7

Conflict of interest

The authors declare that the research was conducted in the absence of any commercial or financial relationships that could be construed as a potential conflict of interest.

Publisher's note

All claims expressed in this article are solely those of the authors and do not necessarily represent those of their affiliated organizations, or those of the publisher, the editors and the reviewers. Any product that may be evaluated in this article, or claim that may be made by its manufacturer, is not guaranteed or endorsed by the publisher.

Supplementary material

The Supplementary Material for this article can be found online at: <https://www.frontiersin.org/articles/10.3389/feart.2022.1033124/full#supplementary-material>

- Guillot, S., Mahéo, G., De Sigoyer, J., Hattori, K. H., and Pêcher, A. (2008). Tethyan and Indian subduction viewed from the Himalayan high-to ultrahigh-pressure metamorphic rocks. *Tectonophysics* 451 (1-4), 225-241. doi:10.1016/j.tecto.2007.11.059
- Guo, C. Y., Zhang, W. Z., Ge, L. S., Gao, B. F., and Xia, R. (2011). Several questions on tracing ore forming fluid by using hydrogen and oxygen isotope system. *Mineralogy Petrology* 31 (03), 41-47. doi:10.19719/j.cnki.1001-6872.2011.03.007
- Heyl, A. V., Landis, G. P., and Zartman, R. E. (1974). Isotopic evidence for the origin of Mississippi valley-type mineral deposits: A review. *Econ. Geol.* 69 (6), 992-1006. doi:10.2113/gsecongeo.69.6.992
- Hou, Z. Q., Qu, X. M., Yang, Z. S., Meng, X. J., Li, Z. Q., Yang, Z. M., et al. (2006). Metallogenesis in Tibetan collisional orogenic belt: III. Mineralization in post-collisional extension setting. *Mineral. Deposits* 25 (6), 629-651. doi:10.16111/j.0258-7106.2006.06.001
- Hou, Z. Q., and Zhang, H. R. (2015). Geodynamics and metallogeny of the eastern tethyan metallogenic domain. *Ore Geol. Rev.* 70, 346-384. doi:10.1016/j.oregeorev.2014.10.026
- Hu, R. Z., Bi, X. W., Jiang, G. H., Chen, H. W., Peng, J. T., Qi, Y. Q., et al. (2012). Mantle-derived noble gases in ore-forming fluids of the granite-related Yaogangxian tungsten deposit, southeastern China. *Miner. Deposita* 47 (6), 623-632. doi:10.1007/s00126-011-0396-x
- Hu, R. Z., Bi, X. W., and Turner, G. P. B. (1999). He and Ar isotope geochemistry of gold ore-forming fluids in Ailaoshan Gold belt. *Sci. China (Series D: Earth Sci.)* 29 (04), 321-330. (in Chinese).
- Hu, R. Z., Burnard, P. G., Bi, X. W., Zhou, M. F., Peng, J. T., Su, W. C., et al. (2004). Helium and argon isotope geochemistry of alkaline intrusion-associated gold and copper deposits along the Red River-Jinshajiang fault belt, SW China. *Chem. Geol.* 203 (3-4), 305-317. doi:10.1016/j.chemgeo.2003.10.006
- Hu, R. Z., Burnard, P. G., Bi, X. W., Zhou, M. F., Peng, J. T., Su, W. C., et al. (2009). Mantle-derived gaseous components in ore-forming fluids of the Xiangshan uranium deposit, Jiangxi Province, China: Evidence from He, Ar and C isotopes. *Chem. Geol.* 266 (1-2), 86-95. doi:10.1016/j.chemgeo.2008.07.017
- Hu, X. M., Garzanti, E., Wang, J. G., Huang, W. T., An, W., and Webb, A. (2016). The timing of India-Asia collision onset-facts, theories, controversies. *Earth Sci. Rev.* 160, 264-299. doi:10.1016/j.earscirev.2016.07.014
- Huang, Y., Cao, H. W., Li, G. M., Brueckner, S. M., Zhang, Z., Dong, L., et al. (2018). Middle-late Triassic bimodal intrusive rocks from the Tethyan Himalaya in South Tibet: Geochronology, petrogenesis and tectonic implications. *Lithos* 318-319, 78-90. doi:10.1016/j.lithos.2018.08.002
- Kali, E., Leloup, P. H., Arnaud, N., Mahéo, G., Liu, D., Boutonnet, E., et al. (2010). Exhumation History of the deepest central Himalayan rocks, AmaDrime range-key Pressure-Temperature-Deformation-Time constraints on orogenic models. *Tectonics* 29 (2), 1-31. doi:10.1029/2009tc002551
- Kendrick, M. A., Burgess, R., Patrick, R. A. D., and Turner, G. (2001). Fluid inclusion noble gas and halogen evidence on the Origin of Cu-porphyr mineralising fluids. *Geochim. Cosmochim. Acta* 65 (16), 2651-2668. doi:10.1016/S0016-7037(01)00618-4
- Kohn, M. J. (2014). Himalayan metamorphism and its tectonic implications. *Annu. Rev. Earth Planet. Sci.* 42 (1), 381-419. doi:10.1146/annurev-earth-060313-055005
- Li, B. L., Wang, L. Q., Zhang, X. G., Pingcui, D. J., Gao, T., and Wang, Y. (2022). Sulfur and lead isotope compositions and their geological significances in the quzhen Sb mineralization section of the Hamuqu Sb-Au deposit, Tibet. *Acta Geosci. Sin.* 43 (2), 202-210.
- Li, C. L., Li, S. R., Yuan, M. W., Du, B. Y., Li, W. L., Masroor, A. L. A. M., et al. (2020). Genesis of the keluo Au deposit in the nenjiang-heihe tectonic mélange belt, heilongjiang province: Evidence from chemical composition and pyrite He-Ar, S, Pb isotopes. *Earth Sci. Front.* 27 (5), 099-115. doi:10.13745/j.esf.2020.5.37
- Li, G. M., Zhang, L. K., Jiao, Y. J., Xia, X. B., Dong, S. L., Fu, J. G., et al. (2017). First discovery and implications of Cuonadong superlarge Be-W-Sn polymetallic deposit in Himalayan metallogenic belt, southern Tibet. *Mineral. Deposits* 36 (04), 1003-1008. doi:10.16111/j.0258-7106.2017.04.014
- Li, G. Q., Gu, X. X., Cheng, W. B., Zhang, Y. M., Zhang, Y., Dai, H. Z., et al. (2014). The analysis of metallogenic material sources of the Zhaxikang antimony (sulfur salts) polymetallic deposits in Southern Tibet: Concurrent discussion on the differences of the ore sources of major mineral deposits in North Himalayan metallogenic belt. *Earth Sci. Front.* 21 (5), 090-104. doi:10.13745/j.esf.2014.05.008
- Li, H., Danišik, M., Zhou, Z. K., Jiang, W. C., and Wu, J. H. (2020b). Integrated U-Pb, Lu-Hf and (U-Th)/He analysis of zircon from the Banxi Sb deposit and its implications for the low-temperature mineralization in South China. *Geosci. Front.* 11, 1323-1335. doi:10.1016/j.gsf.2020.01.004
- Li, H., Kong, H., Guo, B. Y., Soh Tamehe, L., Zhang, Q., Wu, Q. H., et al. (2020a). Fluid inclusion, H-O-S isotope and rare Earth element constraints on the mineralization of the Dong'an Sb deposit, South China. *Ore Geol. Rev.* 126, 103759. doi:10.1016/j.oregeorev.2020.103759
- Li, H., Kong, H., Zhou, Z. K., Tindell, T., Tang, Y. Q., Wu, Q. H., et al. (2019). Genesis of the Banxi Sb deposit, South China: Constraints from wall-rock geochemistry, fluid inclusion microthermometry, Rb-Sr geochronology, and H-O-S isotopes. *Ore Geol. Rev.* 115, 103162. doi:10.1016/j.oregeorev.2019.103162
- Li, H., Wu, Q. H., Evans, N. J., Zhou, Z. K., Kong, H., Xi, X. S., et al. (2018). Geochemistry and geochronology of the Banxi Sb deposit: Implications for fluid origin and the evolution of Sb mineralization in central-Western Hunan, South China. *Gondwana Res.* 55, 112-134. doi:10.1016/j.gr.2017.11.010
- Li, H., Zhu, D. P., Shen, L. W., Algeio, T. J., and Elatikpo, S. M. (2022). A general ore formation model for metasediment-hosted Sb-(Au-W) mineralization of the Woxi and Banxi deposits in South China. *Chem. Geol.* 607, 121020. doi:10.1016/j.chemgeo.2022.121020
- Li, J. G. (2000). *Study on composite Sedex type Antimony and copper deposits in Mesozoic continental margin of central and southern Tibet (thesis)*. Chengdu, China: Chengdu University of Technology.
- Li, J. J., Li, J., Liu, H. B., Zhang, J., Jin, G. S., Zhang, J. F., et al. (2015). Helium isotope composition of inclusions in mineral grains using Helix SFT noble gas mass spectrometer. *Acta Geol. Sin.* 89 (10), 1826-1831.
- Li, Y., Wang, D. H., Wang, C. H., Sun, Y., and Mima, P. C. (2021). Geology and geochemistry of selected gold deposits in the ailaoshan metallogenic belt, China: Origin of ore-forming fluids. *Minerals* 11 (11), 1276. doi:10.3390/min11111276
- Liang, W. (2019). Characteristics of Ore-Forming fluids in Himalayan Au-Sb-Pb-Zn polymetallic belt: Constraints from H-O isotopes. *Earth Sci.* 44 (7), 2308-2321. doi:10.3799/dqkx.2019.172
- Liang, W. (2014). *Metallogenesis of Au-Sb-Pb-Zn mineralization in Tethys Himalaya belt, south Tibet, China (thesis)*. Beijing: China University of Geosciences.
- Liang, W., Zhang, L. K., Xia, X. B., Ma, G. T., Huang, Y., Zhang, Z., et al. (2018). Geology and preliminary mineral genesis of the Cuonadong W-Sn polymetallic deposit, southern Tibet, China. *Earth Sci.* 43 (08), 2742-2754. doi:10.3799/dqkx.2018.154
- Liu, H., Li, G. M., Huang, H. X., Xiao, W. F., Yan, G. Q., Ma, D. F., et al. (2018). Sources of ore-forming materials in the shangxu orogenic gold deposit, northern xizang (tibet): Constraints from C, S, and Pb isotopes. *Geol. Rev.* 64 (05), 1285-1301. doi:10.16509/j.georeview.2018.05.019
- Liu, T., Tian, S. H., Wang, D. H., Hou, K. J., Zhang, Y. J., Li, X. F., et al. (2021). Characteristics of ore-forming fluids in kalu'an hard-rock-type lithium deposit in xinjiang province, China: Evidence from He-Ar isotopes. *Geol. Rev.* 67 (06), 1697-1708. doi:10.16509/j.georeview.2021.06.021
- Lou, Y. L., Chen, W., Yuan, Y. S., and Yang, T. (2018). Fluid inclusion and H, O, and S isotopic composition of Qiaga stibnite deposit in Longzi County, Tibet. *Mineral. Deposits* 37 (5), 1124-1140. doi:10.16111/j.0258-7106.2018.05.014
- Ma, Z. N., Han, Z. P., Li, Y. L., Bi, W. J., Xu, T. K., and Xiao, S. Q. (2022). Exhumation history of the Kampa dome in the southern Tibet: Evidence from low temperature thermochronology. *Sediment. Geol. Tethyan Geol.* 42, 300-309. doi:10.19826/j.cnki.1009-3850.2022.04009
- Mamyrin, B. A., and Tolstikhin, I. N. (1984). *Helium isotopes in nature*. New York: Elsevier Science Publishers.
- Mao, J. W., and Li, X. F. (2004). Mantle-derived fluids in relation to ore-forming and oil-forming processes. *Mineral. Deposits* 23 (4), 520-532. doi:10.16111/j.0258-7106.2004.04.013
- Martin, A. J. (2017). A review of definitions of the Himalayan main central thrust. *Int. J. Earth Sci.* 106 (6), 2131-2145. doi:10.1007/s00531-016-1419-8
- Marty, B., Jambon, A., and Sano, Y. (1989). Helium isotopes and CO₂ in volcanic gases of Japan. *Chem. Geol.* 76 (1-2), 25-40. doi:10.1016/0009-2541(89)90125-3
- McDougall, I., Mac Dougall, I., and Harrison, T. M. (1999). *Geochronology and thermochronology by the ⁴⁰Ar/³⁹Ar method*. Oxford, United Kingdom: Oxford University Press on Demand, 1-269.
- Meng, X. J., Yang, Z. S., Qi, X. X., Hou, Z. Q., and Li, Z. Q. (2008). Silicon-oxygen-hydrogen isotopic compositions of Zaxikang antimony polymetallic deposit in southern Tibet and its responses to the ore-controlling structure. *Acta Petrol. Sin.* 24 (7), 1649-1655.
- Miao, H. Q., Li, G. M., Zhang, Z., Xia, B. B., and Liang, W. (2017). Origin of the Keyue Pb-Zn polymetallic deposit in southern Xizang: Evidences from sulfur and lead isotopic compositions. *Sediment. Geol. Tethyan Geol.* 37 (2), 14-22.
- Nie, F. J., Hu, P., Jiang, S. H., Li, Z. X., Liu, Y., and Zhou, Y. Z. (2005). Type and temporal-spatial distribution of gold and antimony deposits (prospects) in southern Tibet, China. *Acta Geol. Sin.* 79 (03), 373-385.
- Ohmoto, H. (1972). Systematics of sulfur and carbon isotopes in hydrothermal ore deposits. *Econ. Geol.* 67 (5), 551-578. doi:10.2113/gsecongeo.67.5.551
- Olierook, H. K. H., Jiang, Q., Jourdan, F., and Chiaradia, M. (2019). Greater Kerguelen large igneous province reveals no role for Kerguelen mantle plume in the continental breakup of eastern Gondwana. *Earth Planet. Sci. Lett.* 511, 244-255. doi:10.1016/j.epsl.2019.01.037
- Pan, G. T., Wang, L. Q., Yin, F. G., Geng, Q. R., Li, G. M., and Zhu, D. C. (2022). Researches on geological tectonic evolution of Tibetan plateau: A review, recent advances, and directions in the future. *Sediment. Geol. Tethyan Geol.* 42, 151-175. doi:10.19826/j.cnki.1009-3850.2022.05004
- Patterson, D. B., Honda, M., and McDougall, I. (1994). Noble gases in mafic phenocrysts and xenoliths from New Zealand. *Geochimica Cosmochimica Acta* 58 (20), 4411-4427. doi:10.1016/0016-7037(94)90344-1
- Porcelli, D. R., O'Nions, R. K., Galer, S. J. G., Cohen, A. S., and Matthey, D. P. (1992). Isotopic relationships of volatile and lithophile trace elements in continental ultramafic xenoliths. *Contributions Mineralogy Petrology* 110 (4), 528-538. doi:10.1007/bf00344086

- Qi, X. X., Li, T. F., Meng, X. J., and Yu, C. L. (2008). Cenozoic tectonic evolution of the Tethys Himalaya foreland fault-fold belt in southern Tibet, and its constraint on antimony-gold polymetallic mineralogenesis. *Acta Petrol. Sin.* 24 (7), 1638–1648.
- Qiu, H. N. (1996). ^{40}Ar - ^{39}Ar dating of the quartz sample from two mineral deposits in Western Yunnan (SW China) by crushing in vacuum. *Chem. Geol.* 127 (1-3), 211–222. doi:10.1016/0009-2541(95)00093-3
- Qu, X. M., Hou, Z. Q., and Li, Y. G. (2002). Implications of S and Pb isotopic compositions of the Gangdise porphyry copper belt for the ore-forming material source and material recycling within the orogenic belt. *Geol. Bull. China* 21 (11), 768–776.
- Qu, X. M., Hou, Z. Q., and Zhang, Q. L. (2003). *The report of prospective value of Cu, Au, Sb poly-metallic mineral resources in Tibet*. CAGS: Unpublished open-file report, Institute of Mineral Resources, 194. (in Chinese).
- Reid, M. R., and Graham, D. W. (1996). Resolving lithospheric and sub-lithospheric contributions to helium isotope variations in basalts from the southwestern US. *Earth Planet. Sci. Lett.* 144 (1-2), 213–222. doi:10.1016/0012-821X(96)00166-5
- Richards, A., Argles, T., Harris, N., Parrish, R., Ahmad, T., Darbyshire, F., et al. (2005). Himalayan architecture constrained by isotopic tracers from clastic sediments. *Earth Planet. Sci. Lett.* 236 (3-4), 773–796. doi:10.1016/j.epsl.2005.05.034
- Seal, R. R. (2006). Sulfur isotope geochemistry of sulfide minerals. *Rev. Mineralogy Geochem.* 61 (1), 633–677. doi:10.2138/rmg.2006.61.12
- Searle, M. P. (2019). Timing of subduction initiation, arc formation, ophiolite obduction and India-Asia collision in the Himalaya. *Geol. Soc. Lond., Spec. Publ.* 483, 19–37. doi:10.1144/SP483.8
- Simmons, S. F., Sawkins, F. J., and Schlutter, D. J. (1987). Mantle-derived helium two Peruvian hydrothermal ore deposits. *Nature* 329 (6138), 429–432. doi:10.1038/329429a0
- Stuart, F. M., Burnard, P. G., Taylor, R. P., and Turner, G. (1995). Resolving mantle and crustal contributions to ancient hydrothermal fluids: He-Ar isotopes in fluid inclusions from the dawa W-Mo mineralisation, South Korea. *Geochimica Cosmochimica Acta* 59 (22), 4663–4673. doi:10.1016/0016-7037(95)00300-2
- Stuart, F., Turner, G., and Taylor, R. P. (1994). "He-Ar isotope systematics of fluid inclusions: Resolving mantle and crustal contributions to hydrothermal fluids," in *Noble gas geochemistry and cosmochemistry*. Editor J. Matsuda (Tokyo: Terra Scientific Publishing Company), 261–277.
- Sun, J., Zhou, C., Lu, W., Guo, A. M., Xiao, R., Wei, H. T., et al. (2020). He-Ar-Sr isotope geochemistry of ore-forming fluids in the gutaishan Au-Sb deposit in hunan province and its significance for deep prospecting. *Acta Geosci. Sin.* 41 (2), 267–279. doi:10.3975/cagsb.2020.021101
- Sun, X., Wei, H., Zhai, W., Shi, G., Liang, Y., Mo, R. W., et al. (2016). Fluid inclusion geochemistry and Ar-Ar geochronology of the Cenozoic Bangbu orogenic gold deposit, southern Tibet, China. *Ore Geol. Rev.* 74, 196–210. doi:10.1016/j.oregeorev.2015.11.021
- Sun, X., Zheng, Y. Y., Pirajno, F., McCuaig, T. C., Yu, M., Xia, S. L., et al. (2018). Geology, S-Pb isotopes, and $^{40}\text{Ar}/^{39}\text{Ar}$ geochronology of the Zhaxikang Sb-Pb-Zn-Ag deposit in southern Tibet: Implications for multiple mineralization events at Zhaxikang. *Miner. Deposita* 53 (3), 435–458. doi:10.1007/s00126-017-0752-6
- Turner, G., and Stuart, F. M. (1992). Helium/heat ratios and deposition temperatures of sulphides from the ocean floor. *Nature* 357 (6379), 581–583. doi:10.1038/357581a0
- Turner, G., and Wang, S. S. (1992). Excess argon, crustal fluids and apparent isochrons from crushing K-Feldspar. *Earth Planet. Sci. Lett.* 110 (1-4), 193–211. doi:10.1016/0012-821X(92)90048-Z
- Wang, C. L., Huang, H., Tong, X. X., Zheng, M. T., Peng, Z. D., Nan, J. B., et al. (2016). Changing provenance of late Neoproterozoic metasedimentary rocks in the Anshan-Benxi area, North China Craton: Implications for the tectonic setting of the worldclass Dataigou banded iron formation. *Gondwana Res.* 40, 107–123. doi:10.1016/j.gr.2016.08.010
- Wang, D. H. (2019b2019). Discussion on issues related to strategic key mineral resources. *Geol. Chem. Minerals* 41 (2), 65–72.
- Wang, D. H. (2019a). Study on critical mineral resources: Significance of research, determination of types, attributes of resources, progress of prospecting, problems of utilization, and direction of exploitation. *Acta Geol. Sin.* 93 (6), 1189–1209. doi:10.19762/j.cnki.dizhixuebao.2019186
- Wang, D., Sun, X., Zheng, Y. Y., Wu, S., Xia, S. L., Chang, H. F., et al. (2017). Two pulses of mineralization and Genesis of the Zhaxikang Sb-Pb-Zn-Ag deposit in southern Tibet: Constraints from Fe-Zn isotopes. *Ore Geol. Rev.* 84, 347–363. doi:10.1016/j.oregeorev.2016.12.030
- Wang, D., Zheng, Y. Y., Zhang, J. F., Wu, S., Zhang, S. K., Yu, M., et al. (2020). The Sr-He-Ar isotopic and elemental evidence constraints on the ore Genesis of the Zhaxikang Sb-Pb-Zn-Ag deposit in southern Tibet. *Geol. J.* 55 (4), 2631–2645. doi:10.1002/gj.3537
- Wen, C. Q., Duo, J., Fan, X. P., Hu, X. C., Li, B. H., Sun, Y., et al. (2006). Characteristics of ore fluids of the Mayum gold deposit, Western Tibet, China. *Geol. Bull. China* 25 (1), 261–266.
- Wu, F. Y., Liu, Z. C., Liu, X. C., and Ji, W. Q. (2015). Himalayan leucogranite: Petrogenesis and implications to orogenesis and plateau uplift. *Acta Petrol. Sin.* 31 (1), 1–36.
- Xie, Y. L., Li, L. M., Wang, B. G., Li, G. M., Liu, H. F., Li, Y. X., et al. (2017). Genesis of the Zhaxikang epithermal Pb-Zn-Sb deposit in southern Tibet, China: Evidence for a magmatic link. *Ore Geol. Rev.* 80, 891–909. doi:10.1016/j.oregeorev.2016.08.007
- Yang, Z. S., Hou, Z. Q., Gao, W., Wang, H. P., Li, Z. Q., Meng, X. J., et al. (2006). Metallogenic characteristics and genetic model of antimony and gold deposits in south Tibetan detachment system. *Acta Geol. Sin.* 80 (09), 1377–1391.
- Yang, Z. S., Hou, Z. Q., Meng, X. J., Liu, Y. C., Fei, H. C., Tian, S. H., et al. (2009). Post-collisional Sb and Au mineralization related to the South Tibetan detachment system, Himalayan orogen. *Ore Geol. Rev.* 36 (1-3), 194–212. doi:10.1016/j.oregeorev.2009.03.005
- Yin, A. (2006). Cenozoic tectonic evolution of the Himalayan orogen as constrained by along-strike variation of structural geometry, exhumation history, and foreland sedimentation. *Earth Sci. Rev.* 76, 1–131. doi:10.1016/j.earscirev.2005.05.004
- Yin, A., and Harrison, T. M. (2000). Geologic evolution of the Himalayan-Tibetan orogen. *Annu. Rev. Earth Planet. Sci.* 28 (1), 211–280. doi:10.1146/annurev.earth.28.1.211
- Zhai, W., Sun, X. M., Yi, J. Z., Zhang, X. G., Mo, R. W., Zhou, F., et al. (2014). Geology, geochemistry, and genesis of orogenic gold-antimony mineralization in the Himalayan orogen, south Tibet, China. *Ore Geol. Rev.* 58, 68–90. doi:10.1016/j.oregeorev.2013.11.001
- Zhai, W., Zheng, S. Q., Sun, X. M., Wei, H. X., Mo, R. W., Zhang, L. Y., et al. (2018). He-Ar isotope compositions of orogenic Mazhala Au-Sb and Shalagang Sb deposits in Himalayan orogeny, southern Tibet: Constrains to ore-forming fluid origin. *Acta Petrol. Sin.* 34 (12), 3525–3538.
- Zhang, G. Y. (2012). *Metallogenic model and prospecting potential in southern Tibet Au-Sb polymetallic belt (thesis)*. Wuhan: China University of Geosciences.
- Zhang, J. F., Zheng, Y. Y., Zhang, G. Y., Gao, S. B., Ye, X. R., Zhang, Z., et al. (2010). Genesis of Zhaxikang Pb-Zn-Sb-Ag deposit in northern Himalaya: constraints from multi-isotope geochemistry. *Earth Science-Journal China Univ. Geosciences* 35 (6), 1000–1010. doi:10.3799/dqkx.2010.113
- Zhang, J. J., Santosh, M., Wang, X. X., Guo, L., Yang, X. Y., and Zhang, B. (2012). Tectonics of the northern Himalaya since the India-Asia collision. *Gondwana Res.* 21 (4), 939–960. doi:10.1016/j.gr.2011.11.004
- Zhang, K. J., Xia, B. D., Wang, G. M., Li, Y. T., and Ye, H. F. (2004). Early Cretaceous stratigraphy, depositional environments, sandstone provenance, and tectonic setting of central Tibet, Western China. *Geol. Soc. Am. Bull.* 116 (9-10), 1202–1222. doi:10.1130/B25388.1
- Zhang, K. J., Zhang, Y. X., Li, B., and Zhong, L. F. (2007). Nd isotopes of siliciclastic rocks from Tibet, Western China: Constraints on provenance and pre-Cenozoic tectonic evolution. *Earth Planet. Sci. Lett.* 256 (3), 604–616. doi:10.1016/j.epsl.2007.02.014
- Zhang, L. K., Li, G. M., Santosh, M., Cao, H. W., Dong, S. L., Zhang, Z., et al. (2019). Cambrian magmatism in the Tethys Himalaya and implications for the evolution of the proto-tethys along the northern gondwana margin: A case study and overview. *Geol. J.* 54, 2545–2565. doi:10.1002/gj.3311
- Zhang, S. K. (2016). *Geological and geochemical characteristics of Zhaxikang antimony polymetallic deposit, southern tibet(thesis)*. Beijing: China University of Geosciences.
- Zhang, S. Z., Li, J. H., Li, G. D., Zhang, H. B., Gao, X., Wu, L. H., et al. (2005). *Report of 1:250000 Zada county regional geological survey in Tibet*. Hebei: Hebei Institute of Geological Survey. (in Chinese).
- Zheng, Y. Y., Fan, W. Y., Zhang, X. B., Yan, J., Liu, M. Y., Zhang, H. P., et al. (2003). *Geological report on resource investigation and evaluation of Gyantse-Longzi gold and antimony polymetallic metallogenic belt in Tibet*. Lhasa: Geological Survey Institute of Tibet Autonomous Region. (in Chinese).
- Zheng, Y. Y., Liu, M. Y., Sun, X., Yuan, E. H., Tian, L. M., Zheng, H. T., et al. (2012). Type, discovery process and significance of Zhaxikang antimony polymetallic ore deposit, Tibet. *Earth Science-Journal China Univ. Geosciences* 37 (5), 1003–1014. doi:10.3799/dqkx.2012.108
- Zheng, Y. Y., Sun, X., Tian, L. M., Zheng, H. T., Yu, M., Yang, W. T., et al. (2014). Mineralization, deposit type and metallogenic age of the gold antimony polymetallic belt in the eastern part of north Himalayan. *Geotect. Metallogenia* 38 (1), 108–118.
- Zheng, Y. Y., Wang, D., Yi, J. Z., Yu, Z. Z., Jiang, Z. X., Li, X. X., et al. (2022). Antimony mineralization and prospecting orientation in the north Himalayan metallogenic belt, Tibet. *Earth Sci. Front.* 29 (01), 200–230. doi:10.13745/j.esf.sc.2021.8.5
- Zhou, Q., Li, G. M., Xia, X. B., Wu, J. Y., Lai, Y., Li, Y. X., et al. (2014). Metallogenic model of Zhaxikang Pb-Zn polymetallic ore cluster in South Tibet. *Mineral. Deposits* 33 (S1), 353–354. (in Chinese). doi:10.16111/j.0258-7106.2014.s1.179
- Zhou, Q., Li, W. C., Qing, C. S., Lai, Y., Li, Y. X., Liao, Z. W., et al. (2017). Origin and tectonic implications of the Zhaxikang Pb-Zn-Sb-Ag deposit in northern Himalaya: Evidence from structures, Re-Os-Pb-S isotopes, and fluid inclusions. *Miner. Deposita* 53 (4), 585–600. doi:10.1007/s00126-017-0760-6
- Zhu, D. C., Zhao, Z. D., Pan, G. T., Lee, H. Y., Kang, Z. Q., Liao, Z. L., et al. (2009). Early cretaceous subduction-related adakite-like rocks of the Gangdese Belt, southern Tibet: Products of slab melting and subsequent melt-peridotite interaction? *J. Asian Earth Sci.* 34 (3), 298–309. doi:10.1016/j.jseas.2008.05.003
- Zhu, L. K., Gu, X. X., Li, G. Q., Zhang, Y. M., Cheng, W. B., and Bian, X. D. (2012). Fluid inclusions in the Zhaxikang Pb-Zn-Sb polymetallic deposit, south Tibet, and its geological significance. *Geoscience* 26 (3), 453–463.
- Zou, H., Cao, H. W., Bagas, L., Zhang, Y. H., Zhang, S. T., Zhang, Q., et al. (2019). Origin of the Mo-bearing Xiaoshuijing syenogranite in the tengchong terrane, SW China. *Ore Geol. Rev.* 105, 258–272. doi:10.1016/j.oregeorev.2018.12.018
- Zou, H., Fang, Y., Zhang, S. T., and Zhang, Q. (2017). The source of fengjia and langxi barite-fluorite deposits in southeastern sichuan, China: Evidence from rare Earth elements and S, Sr, and Sm-Nd isotopic data. *Geol. J.* 52 (3), 470–488. doi:10.1002/gj.2779